# MICROSTRUCTURE AND TRIBOLOGY OF Fe-Cr-Mo–BASED ALLOY FABRICATED USING SPARK PLASMA SINTERING

BY

**ADEDAYO SHERIFF ADENIYI**

A Thesis Presented to the
DEANSHIP OF GRADUATE STUDIES

**KING FAHD UNIVERSITY OF PETROLEUM & MINERALS**
DHAHRAN, SAUDI ARABIA

In Partial Fulfillment of the
Requirements for the Degree of

**MASTER OF SCIENCE**
**In**

**MATERIALS SCIENCE AND ENGINEERING**

**JANUARY, 2017**

## DEANSHIP OF GRADUATE STUDIES

This thesis, written by ADEDAYO SHERIFF ADENIYI under the direction of his thesis advisor and approved by his thesis committee, has been presented and accepted by the Dean of Graduate Studies, in partial fulfillment of the requirements for the degree of **MASTER OF SCIENCE IN MATERIALS SCIENCE AND ENGINEERING.**

Dr. Zuhair Gasem
Department Chairman

Dr. Salam A. Zummo
Dean of Graduate Studies

9/3/17
Date

AAS
Dr. Ahmad Sorour
(Advisor)

Dr. Tahar Laoui
(Member)

Samad
Dr. Mohammed Abdul Samad
(Member)

*To Almighty Allah, my Lord of infinite compassion. To my beloved parents; Prince Adeniyi Amusa and Mrs. Folasade Adeniyi, my siblings, and to my dearest, my wife; Olanite Huswah, may Allah continue to shower upon you all His mercies and blessings as you have been a source of my happiness.*

# ACKNOWLEDGEMENT

This work was carried out at the King Fahd University of Petroleum and Minerals (KFUPM), Saudi Arabia within a span of two years from 2014 to 2016. I would like to appreciate the Kingdom of Saudi Arabia for the Scholarship which facilitated my MSc. program in KFUPM. The Deanship of Research, KFUPM is greatly appreciated for supporting this research work financially. I would like to thank my supervisor, Dr. Ahmad Sorour for his guidance and support. I am grateful for your inspiration and enthusiasm during this thesis. I admire the way you always found time for valuable help and discussions.

This work would not have been conceivable without the help and direction of many others, and I might hence want to thank everybody included. Firstly, I greatly appreciate my thesis committee members, Dr. Tahar Laoui and Dr. Mohammad Abdul Samad for their immense professional effort in ensuring a good study. Special thanks to a friend and brother, Dr. Mohamed Hussein, for his assistance with spark plasma sintering (SPS) tests, ensuring a study well done. His brotherly advices are really appreciated.

Further, I would like to thank Dr. Abbas Hakeem and Mr. Idris Akolade of the center of nanotechnology (CENT), KFUPM, for the assistance with access to the spark plasma sintering (SPS) equipment; LiquidMetal Technologies for providing the Fe-Cr-Mo based amorphous powders; Umar Azam, Abdulhakeem Baqi, Ismail Aliyu and Abdulhakeem Adesina for the help with the sliding wear tests; Dr. Anwar Ul-Hamid and Hatim Dafalla for assistance with the easy access to SEM and XRD equipment.

I am also very grateful to my colleagues at KFUPM for their support and assistance. To everyone who have in one way assisted during the course of this work, and whose names are not published in this work due to space constraint, my utmost appreciation to you all. Heart felt appreciation to all members of the Nigerian Community University of Petroleum and Minerals. The community has been a platform for ensuring we feel home right here in Saudi Arabia.

Finally and most importantly, I wish to express my deepest gratitude to my love, Olanite Huswah, and my family for your valuable support during the entire MSc study. Without you I would never have finished this thesis.

Dhahran, January 2017

Adedayo Sheriff Adeniyi

# CONTENTS

# LIST OF TABLES

# LIST OF FIGURES

# ABSTRACT

Full Name : ADEDAYO SHERIFF ADENIYI
Thesis Title : Microstructure and Tribology of Fe-Cr-Mo–Based alloy fabricated using Spark Plasma Sintering
Major Field : Materials Science and Engineering
Date of Degree : January, 2017

In the search for anti-wear materials, a wide range of materials have been developed such as the metallic glass and nanocrystalline alloys. Nanocrystalline alloys, for example, have been synthesized via mechanical alloying, electrodeposition and crystallization from amorphous materials. The focal point of this research is using sintering process to fabricate a nanocrystalline material from a metallic glass (amorphous) precursor. The aim of this work is to study the effect of sintering temperature on the densification, microstructure, hardness, and tribological properties of Fe58Cr23Mo15B2C2 (wt. %) alloy fabricated by spark plasma sintering (SPS) of the initial glassy powders. Initial characterizations of the as-received glassy powder was conducted using differential scanning calorimetry (DSC), scanning electron microscope (SEM), and X-ray diffraction (XRD). The results showed that the glass transition temperature Tg, the crystallization temperature Tx, and the melting temperature were 602, 645, and 1150 $^{o}$C, respectively. The metallic glassy powder was then consolidated using SPS equipment at 500, 600, 700, 800, 900, and 1000 $^{o}$C. Microstructure analysis using XRD and field-emission SEM (FE-SEM) equipped with an energy dispersive spectroscope (EDS) showed partial and full crystallization with the formation of $(Fe,Cr)_{23}C_6$ particles and $(Cr,Fe)_2B$ nanoparticles embedded in Fe-based matrix. The tribology behavior of the fully sintered sample was investigated using a ball-on-disk tribometer. The sliding wear tests were also conducted using stainless steel and alumina counterface materials. When compared with conventional materials (carbon steel and D2 tool steel), the sintered samples were seen to have a higher resistance to wear. Also, when the sintered alloy was slid against alumina counterface material, it exhibited a 94% and 72% reduced wear when compared to carbon steel and D2 tool steel respectively. The surface of the worn sample was also analyzed using SEM and EDS, where it was seen that the wear mode was both oxidative and abrasive.

# ملخص الرسالة

الاسم الكامل : أديدايو شريف أدينيي
عنوان الرسالة : البنية المجهرية وترايبولوجي سبائك Fe-Cr-Mo المصنوعة بواسطة تلبد شرارة البلازما
التخصص : الهندسة الميكانيكية
تاريخ الدرجة العلمية : يناير, 2017 ، الموافق ربيع الثاني 1438

في هذا البحث المعني بالمواد المضادة للتآكل، استحدثت مجموعة واسعة من المواد مثل الزجاج المعدني والسبائك النانوبلورية. السبائك النانوبلورية، على سبيل المثال، قد تم تصنيعها عن طريق الخلط الميكانيكي، والترسيب الكهربائي، والتبلور من مواد غير متبلورة. النقطة المحورية في هذا البحث هو استخدام عملية تلبد لصناعة مادة نانوبلورية من زجاج معدني (غير متبلور) سليفة. والهدف من هذا العمل هو دراسة تأثير درجة حرارة التلبد على التكثيف، البنية المجهرية، الصلابة، والخصائص الترابولوجية لسبائك Fe58Cr23Mo15B2C2 (% بالوزن) مصنوعة بتلبد شرارة البلازما (SPS) من مساحيق زجاجية أولية. الأوصاف الأولية للمسحوق الزجاجي كما تلقي استخرجت باستخدام كالوري المسح التفاضلي (DSC) و مجهر المسح الإلكتروني (SEM) وحيود الأشعة السينية (XRD). وأظهرت النتائج أن درجة حرارة التحول الزجاجي $T_g$، درجة حرارة التبلور $T_x$، ودرجة حرارة الذوبان كانت 602، 645، و1150 درجة مئوية على التوالي. ثم عزز المسحوق الزجاجي المعدني باستخدام معدات (SPS) في 500، 600، 700، 800، 900، و 1000 درجة مئوية. تحليل البنية المجهرية باستخدام حيود الأشعة السينية (XRD) و اشعاعات مجال مجهر المسح الإلكتروني (FE-SEM) ومزودة بمطياف الطاقة المشتتة (EDS) أظهر تبلور جزئي وكامل مع تكون جسيمات $(Fe,Cr)_{23}C_6$ ، وجسيمات نانوية من $(Cr, Fe)_2B$ مضمنة في مصفوفة مؤسسة من الحديد. تم التحقق من السلوك الترايبولوجي للعينة الملبدة تماما باستخدام تريبوميتير كرة على قرص استخدام. وأجريت أيضا اختبارات التآكل الانزلاقي باستخدام الفولاذ المقاوم للصدأ ومواد الألومينا في الجهة المقابلة. بالمقارنة مع المواد التقليدية (الفولاذ الكربوني و أداة الصلب B2)، لوحظ أن للعينات الملبدة مقاومة أعلى للتآكل. عندما ازلقت السبيكة الملبدة ضد مادة الألومينا في الجهة المقابلة، اظهرت انخفاض في التآكل بنسبة 94% و 72% في المائة بالمقارنة مع الكربون الصلب وأداة الصلب B2 على التوالي. وكان سطح العينة البالية قد تم تحليله أيضا باستخدام SEM و EDS، حيث شوهد أن طريقة التآكل كانت بالأكسدة والكشط معاً.

# CHAPTER 1

# INTRODUCTION

Owing to the crystalline nature of iron-based alloys, they have found ample usage in applications requiring high strength, corrosion and wear resistance, among others. These alloys have been studied extensively for decades whereas studies into iron-based amorphous alloys started after the first successful synthesis of metallic glass alloys in 1960. Metallic glass (MG) alloys, amongst a variety of recently developed materials, such as nanocrystalline alloys [1,2] and quasi-crystals [3], were first synthesized in 1960 by a rapid solidification process [4]. The high solidification or cooling rate of about $10^6$ K/s is responsible for the disordered arrangement of atoms, and thus the glassy phase is brought about.

As these alloys transform from crystalline to amorphous (during synthesis), or from amorphous to crystalline structure, it is important to investigate their microstructure as this knowledge is key to understanding their macroscopic performance in terms of their properties, which ultimately influences the application of these materials in the industry. Several metallic glass or amorphous alloy systems synthesized in the past have been seen to possess exceptional mechanical properties, magnetic properties, and outstanding corrosion and wear resistant characteristics [5–11]. However, their limited plasticity in tension and the difficulty in processing these novel alloys tend to undermine the vast application as bulk alloys [5,9,12–15].

The crystallization of metallic glass alloys by in-situ or ex-situ introduction of nanocrystalline precipitates has been reported to enhance the tensile ductility of amorphous metals. This has therefore led to increased interests in understanding the crystallization behavior of metallic glass alloys. Many crystallization-based investigations [5,16,17] have been channeled towards adapting the microstructure of these alloys into either a glassy-nanocrystalline, fine-grained composite or an entirely crystalline material by controlling the time and temperature of devitrification. Although many techniques have been used to produce nanocrystalline materials from amorphous powders, a novel powder metallurgy method that can produce high-density sintered products at low temperatures has been gaining increasing popularity. This method is called spark plasma sintering (SPS), and it involves the concurrent exertion application of pulsed direct electric current and uniaxial pressure to consolidate powder materials into bulk part [18,19].

A good comprehension of how metallic glassy alloys transform from amorphous to fully or partially crystalline structure is now indispensable in order to optimize the properties and performance of this novel material. For example, in tribology, and especially in applications requiring structural materials, it is important to have materials that have high ductility in tension due to formability and safety of structural components. The precipitation of fine crystalline phase particles within bulk metallic glassy (BMG) alloys matrix can be used to improve their ductility. Starting from fully non-crystalline materials portrays itself as a means to obtain such novel microstructures and properties. An example of a promising alloy system is an iron based BMG. They have been described to possess superb soft magnetic properties, high mechanical resistivity, high mechanical strength and less expensive [10]. The Fe-based MG alloy for example present itself as a good starting material to study their properties upon crystallization.

From the tribology point of view, the introduction of partial crystalline phases has been reported to improve the wear properties of the Fe-based MG alloys and coatings [20–23]. These improved properties have been linked to fine grain strengthening and enhancement of their toughness. The starting alloy investigated in this thesis was Fe-26Cr-17Mo-2C-2B (wt. %) MG powder. The densification behavior, phase evolution and tribology performance is studied after bulk consolidation using a unique and novel spark plasma sintering (SPS) technique.

## Outline

This thesis is presented in the conventional monograph style and contains six chapters. **Chapter 1** describes the main topic, gives a succinct related background and literature and further states the importance of the current research.

**Chapter 2** describes a comprehensive background and a literature review on spark plasma sintering and tribology of iron based alloy in relation to previous studies.

The aim and objectives of this research was stated in **chapter 3**.

**Chapter 4** presents the experimental methodologies and equipment deployed in details.

The results from the investigations are described in **Chapter 5.** The effect of sintering temperature on the densification behavior, hardness, microstructure, and phase evolution of the sintered samples is presented. Furthermore, the sliding wear performance of the most densified sintered alloy is presented

**Chapter 6** presents the conclusions arrived at based on the results in chapter 6. Proposed future investigations to improve upon this work are suggested.

# CHAPTER 2

# BACKGROUND AND LITERATURE REVIEW

In this chapter, a basic background and an extensive report of previously studied works are described. Section 2.1 provides a background of MG and nanocrystalline advanced alloys. A detailed background on spark plasma sintering (SPS) process used to fabricate these alloys is described in section 2.2. This section also recounts studies where SPS has been used to develop bulk amorphous and nanocrystalline alloys. Section 2.3 describes Fe-based alloys: their synthesis and microstructure. Section 2.4 presents a background on tribology properties of Fe based amorphous and nanocrystalline alloys.

## 2.1 Advanced Materials

The development of novel materials, and the refinement to already existing materials in order to obtain materials of higher-grade performance for present day industrial and scientific applications, have been the major preoccupation of material scientists. Advanced materials such as quasicrystals [24,25], metal matrix composites [26], nanocrystalline materials [27,28], and metallic glasses [29–31], among others have been developed. These materials have been developed via several processing techniques and a large amount of database exist for all these materials. But this work will focus on metallic glass materials and the development of nanocrystalline alloys from these materials.

### 2.1.1 Metallic Glass Alloys

The history of metals and metallic alloys dates back to decades before that of iron age [32]. These materials are generally polycrystalline in structure having their atoms arranged in a repetitive pattern in three dimensions [33]. These materials when cooled from their liquid melt decrease in volume with reduction in temperature until a sudden drop in its specific volume is reached after which a solid material is formed. If however, heterogeneous crystal forming sites are removed or the molten liquid is rapidly solidified far below the melting temperature, a glass may be formed. It was based upon this principle of rapid solidification processing (RSP) [33] that Duwez and his team synthesized binary alloy, $Au_{75}Si_{25}$, the first ever reported metallic glass [4]. The material is non crystalline or amorphous in structure and this was achieved as a result of the insufficient time the atoms of the material had to rearrange themselves for crystal growth [7]. The excellent properties (as shown in figure 2.1) which these novel alloys possess over traditional materials could be attributed to their defect-free nature.

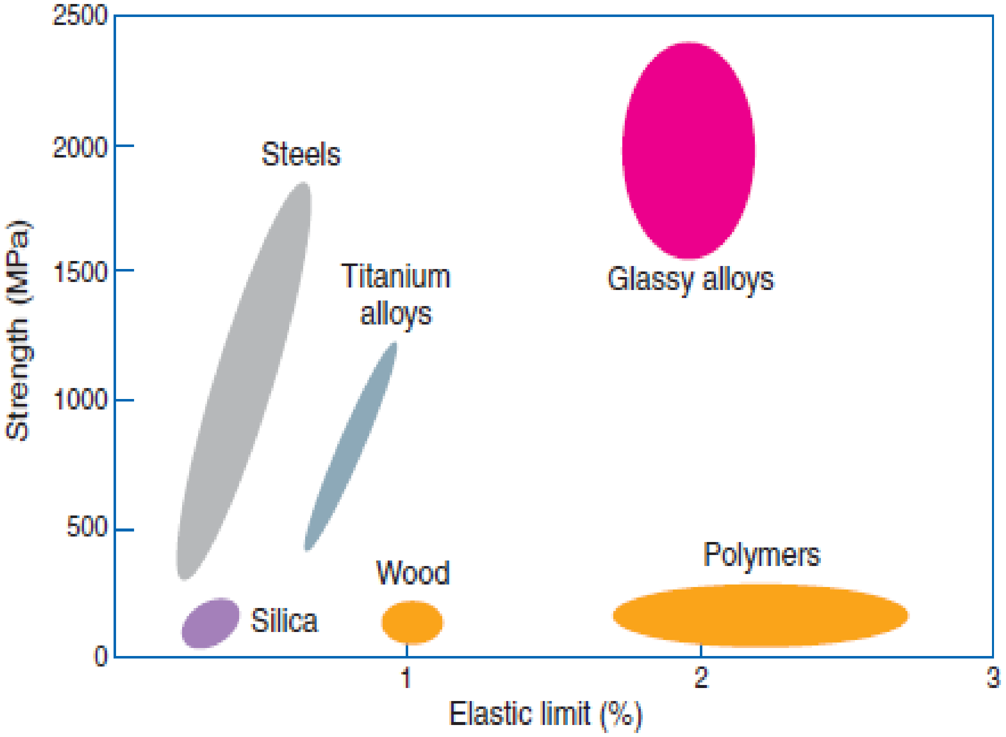

Figure 2.1. Strength and elastic limit of different materials [7]

### 2.1.2 Nanocrystalline Materials

The history of nanomaterials began in 1959 when Feyman spoke about the development of molecular machines atom by atom, while the term molecular nanotechnology was coined by Eric Drexler in 1977. A nanocrystalline material is defined as that with single or multi-phase multi-crystals, and whose crystal sizes ranges between 1–250 nm, while ultra-fine sized multi-crystals is often used for materials with grain sizes between 250–1000 nm [28]. On a microstructural level, a sizeable volume fraction of the interfaces which exist between two crystallites is observed in nanosized crystalline materials, and this appreciably makes changes to many of their properties when compared to coarse-grained multi-crystalline materials [3,34,35].

Research interests in developing amorphous and nanocrystalline materials having magnetic properties that make them applicable in electrical devices as increased rapidly. Developing nanocrystalline materials having soft magnetic properties has been a recent development in the field of nanotechnology. This is partly because these amorphous and crystalline materials possess excellent properties when compared to conventional multi-crystalline materials. Due to these excellent properties, there has been a rise in the need for several synthesis methods for these materials.

## 2.2 Processing of Metallic Glass and Nanocrystalline Alloys

One major route in which metallic glasses have been processed is the non-equilibrium rapid solidification processing technique. Other non-equilibrium processing techniques used to produce these glassy alloys are mechanical milling, electrodeposition, and vapor deposition. Through these methods, metallic glasses have been developed into structurally insignificant products such as powders, thin foils, wires and ribbons with a section thickness of about 1 mm [13]. For example Choi et al. [36], developed various Al-based amorphous powders after long hours of  high energy ball milling. The noncrystalline structure of this alloy was confirmed using transmission electron microscopy (TEM), differential scanning calorimetry (DSC) and x-ray diffraction (XRD) techniques. Similar method was also used by Neamtu at al. [37], to synthesize amorphous $Fe_{75}Si_{20}B_5$ powders. The fingerprint which sets metallic glassy alloy from crystalline alloy when evaluated using XRD technique is the presence of a broad diffuse peak. Furthermore to the synthesis of amorphous alloys, Jung et al. [38], Balla and Bandyopadhyay [39] confirmed an amorphous phase from Fe-based laser processed alloys. This limitation in size has partly sparked an interest in materials scientists and engineers to synthesize these alloys via other routes and also fabricating them to obtain bulk amorphous samples commonly known as bulk metallic glass (BMG). Several solidification processing routes [1] such as casting and powder metallurgy techniques have been used to develop these bulk amorphous materials. During material processing, much emphasis is given to design issues in order to obtain the desired material. For example processing metallic glasses alloy into bulk amorphous alloys, four conditions need to be met [7,33]:

- The alloy system must be a multicomponent system such that the minimum number of element that makes up the system exceeds three. The higher the number of components, the lower the energy required for atomic ordered arrangement.
- The critical solidification rate at which they may be synthesized must be as low as 1000K/s. This limits the possibility or extent of crystallization.
- Diameters or the large section thickness of BMGs is about 1mm and above.
- BMGs have a characteristic large supercooled liquid region (SLR), and this is defined as the difference between the glass transition temperature $T_g$ and the temperature of crystallization, $T_x$ i.e. large $\Delta T_x = T_x - T_g$.

Nanocrystalline alloys on the other hand may be synthesized by several means such as inert gas condensation, mechanical alloying, electrodeposition, crystallization from amorphous material, severe plastic deformation, cryomilling, plasma synthesis, chemical vapor deposition, pulse electron deposition, sputtering, physical vapor deposition, and spark erosion [1–3,27,28,40]. This work will be focused on nanocrystalline material development from amorphous precursors. This is because the materials developed through this means are a starting point for understanding the crystallization behavior of metallic glasses. Furthermore, starting with metallic glass alloy may bring about unique and novel microstructures. Nanocrystalline materials can be developed by the controlled devitrification of metallic glassy or amorphous materials. In reality, the most frequent technique to develop nanocrystalline magnetic materials has been to initially produce a metallic glass through rapid solidification processes, after which the amorphous phase of the material is slowly crystallized [2]. This technique, which has now gained ground as an effective means to produce nanostructured material was first used by Yoshizawa [41] to produce an iron based nanocrystalline material in what is now known as FINEMET. Iron based alloy developed through this means have been extensively studied for their magnetic properties.

A sizeable amount of nanosized multi-crystalline alloys of various alloy compositions have been successfully synthesized by crystallizing amorphous precursors [42–45]. The partial or total crystallization of amorphous materials is a promising technique for the development of nanocrystalline materials due to the ability to control the microstructure. The amorphous solids are in thermodynamic metastable state and they transform into more stable states under appropriate circumstances. The driving force for the crystallization is the difference in the Gibbs free energy between the amorphous and crystalline states. Usually, amorphous solids may crystallize into polycrystalline phases when they are subjected to heat treatment [21], irradiation [46], or even mechanical alloying [47]. Of these techniques, conventional thermal annealing is most commonly utilized in investigations of amorphous solids.

Non-conventional consolidation methods for densification of nanocrystalline particulates include microwave sintering, field assisted sintering methods, and shockwave consolidation [40]. The field assisted sintering technology (FAST), also known as spark plasma sintering is a powder metallurgy technique that can be used to develop nanocrystalline alloys from amorphous precursors. This process brings together the advantage of thermal annealing and the ability of fabricating very high dense bulk sample.

### 2.2.1 Spark Plasma Sintering

Sintering, which involves consolidating powders into bulk form, is a fabrication process whereby powder particles are bonded by the diffusion of atoms to bring about densification. Sintering has been in existence for thousands of years. The age-old Mesopotamians as at 6000BC made bricks by sintering [18]. Metallic and ceramic based parts were sintered by Egyptians as at the early years 3000BC. The Incas of South America, between the 14th and 15th century made jewelries by sintering [18]. The empirical advancement in the art of sintering further developed solid state sintering during the first half of the 19th century [18].

Before the advent of the SPS process, hot pressing (HP) as well as hot isostatic pressing (HIP) processing techniques have been used for sintering. In 1955, Dayton and his colleagues at the Battelle Memorial institute, United States of America (USA) developed the HIP method of sintering [19]. The motive behind developing the HIP was to develop nuclear fuel elements by diffusion bonding. HIP is a pressure sintering method. Beryllium powder was the first powder to be sintered using HIP, after which further advancements were made to sinter hard alloys with HIP [19]. The birth of spark sintering was as a result of the search for a means to activate the sintering process. Electrical current as a means to facilitate the sintering of powders was a major breakthrough. Although research using electrical energy to energize sintering started as at the late 30s, the Japanese were the first to patent this technology in the 1960s [12].

The role played by the current field on the movement of the particle to be consolidated can be calculated based on the theory of electron-migration, given by the expression [18]:

$$J_i = \frac{D_i C_i}{RT}\left[\frac{RT\partial \ ln C_i}{\partial x} + Fz^* E\right] \qquad (1)$$

$J_i$ represents flux of the diffusing ith specie, $R$, the gas constant, $T$ is the temperature, $D_i$ is the diffusivity of the species, $C_i$ is the concentration of the species, $F$ is the Faraday's constant, $z$ is the total charge of the species diffusing and $E$ is the field. Due to limited field of application of this technique, its efficiency, and cost of the equipment, it was not widely used, not until the development of plasma activated sintering (PAS) and then spark plasma sintering (SPS) [12]. SPS technique can be used to develop a wide range of material classes. The different types of materials that can be sintered by SPS processing is shown in the figure 2.2.

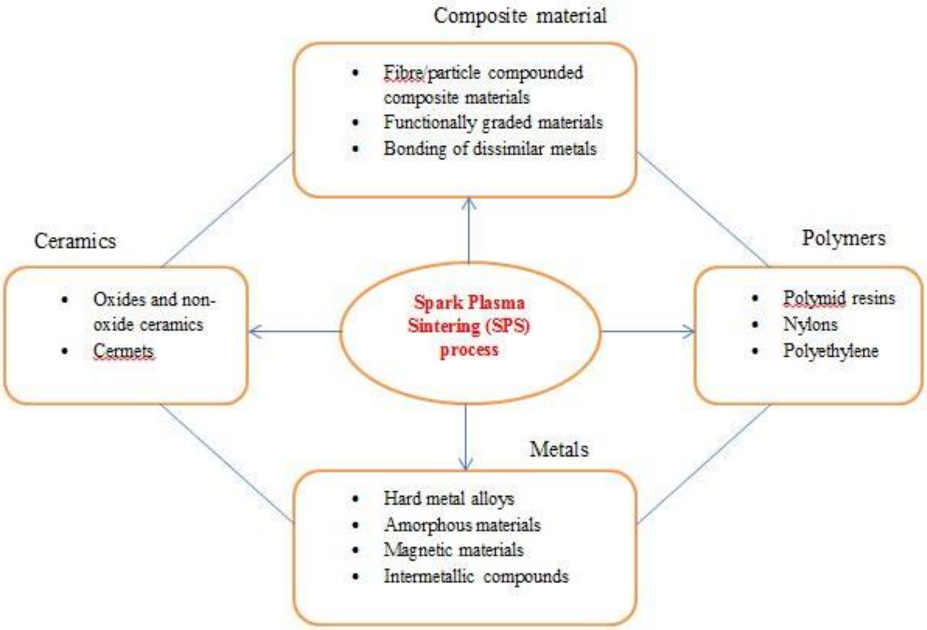

Figure 2.2. Materials that can be sintered via the SPS technique [48]

The SPS processing technique referred to as the field-assisted sintering technology (FAST) is a novel powder consolidation technique. This technique involves the use of pulsed direct electric current (DC), low voltage, with the application of uniaxial force under low atmospheric pressure to consolidate powders in a single step. A schematic of the SPS technique is shown in figure 2.3. During SPS process, the combined effect from the dc electric current and uniaxial pressure enhances sintering [18]. At the onset of sintering, powder to be compacted is placed into a die, the powder is then heated as a result of the pulsed dc current which passes via the die and the powder. The current passed results in Joule effect, which allows accelerated rise in temperature, and further enhances mass transfer [12]. The synergy between joule effect from current passed and applied uniaxial pressure are both responsible for consolidation. The densification is also improved due to surface effect induced by the SPS process [12]. The path of flow of current through the powder during the sintering process and temperature on the surface of the powder particle are shown in the figure 2.4.

With the SPS technique, very high heating and cooling rates can be used. Due to this, densification of green compacts is favored over grain growth thereby increasing diffusion mechanisms and keeping intact the innate properties of powders in their fully dense form [49]. The difference between the FAST/SPS and hot pressing (HP) is observed by the manner of heat production and transfer through the powders [19]. For an electrically conductive green body, energy is expended within the powders and the conductive parts of the pressing tool. Hence, a tool that is conductive is employed and the heat is transmitted by conduction through the powders [19]. It has also been called pulsed electric current sintering (PECS) or plasma activated sintering (PAS) process due to the inability to confirm the existence of spark discharge during sintering [12].

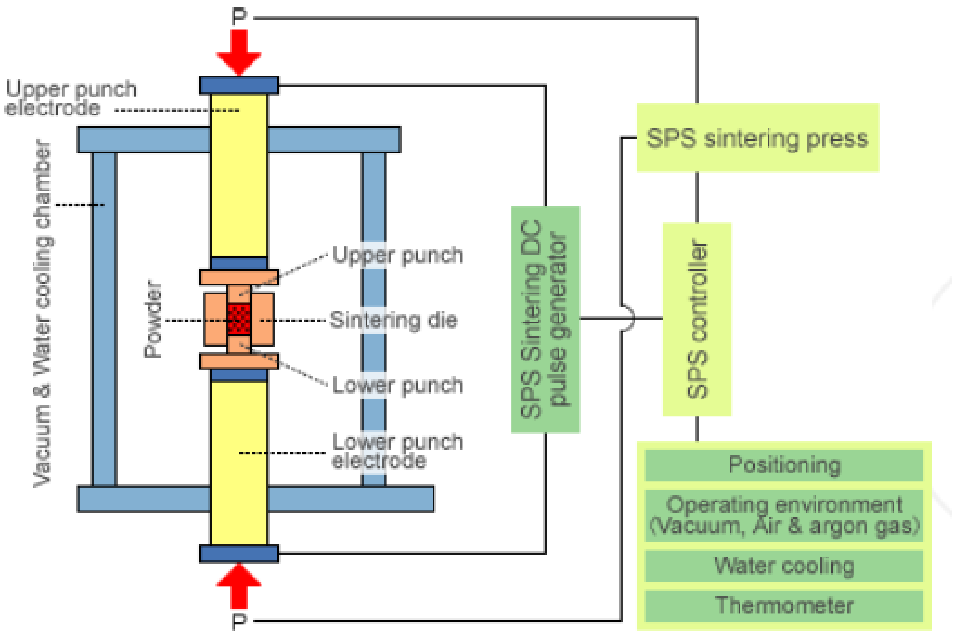

Figure 2.3. Schematic of the spark plasma sintering technique [49]

With the SPS processing technique, powder materials can be sintered at all temperatures and times lower than that of conventional sintering processes. These features allows for synthesizing materials that requires crystallization and grain growth to be suppressed [12]. Some of the important parameters during bulk consolidation by SPS are; temperature, applied uniaxial pressure, heating rate, and dwell time. All these parameters have their unique roles and play a part in the densification of the bulk-sintered alloys.

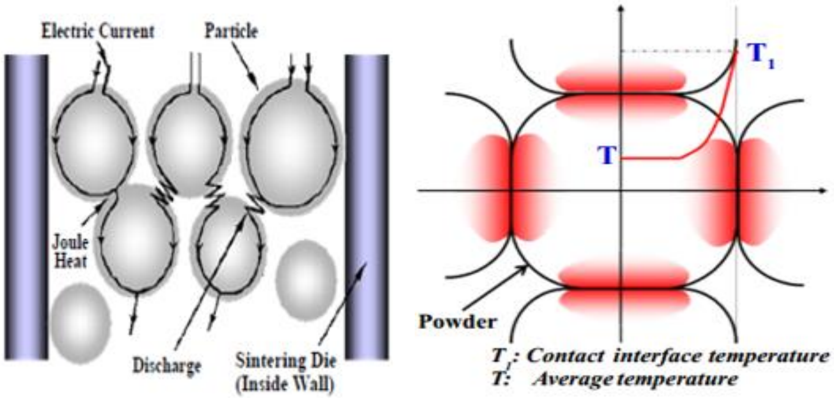

Figure 2.4. Path of electric current flow (a) and surface temperature in powder particles during sintering [12].

### Temperature effects

When compared to other bulk consolidation techniques, the SPS method allows for sintering at lower temperatures. Sintering temperature plays an important role in densification during consolidation by SPS. During sintering, increasing temperature induces some surface effect (eliminates impurities and adsorbed gases on the powder surface), and speeds up the transfer of mass thereby enhancing densification [12]. The relationship between temperature and density of the spark plasma sintered material was proposed by Garay [50].

$$\rho = s\left(\frac{T}{T_m}\right) + b \qquad (2)$$

Where ρ, s, T, $T_m$ and b represents the density, sample temperature sensitivity (the slope from linear plot), sintering temperature, melting temperature and intercept (on the density axis) respectively. From the relationship, it is seen that increasing the sintering temperature will lead to increase in density which in turn means increased densification.

## 2.3 Iron based alloys

### 2.3.1 Synthesis of amorphous and nanostructured alloys

In the previous section, a survey of spark plasma sintering has been explained – the working principles, the nature of material that can be sintered by SPS and the effect of temperature on the properties of the bulk sample have discussed. It should be noted that this process has been used to develop nanostructured materials too. Over the years, several works on the fabrication of various BMGs alloys from MG alloys using SPS have been reported. Examples of such are, Al-based [36,51], Cu-based [52–54], Mg-based [55,56], Ni-based [57–59], Zr-based [60,61] and Fe-based BMGs [62]. From these studies, focus has been made on retaining the amorphous structure of the alloys by sintering below the crystallization temperatures. Also, very high sintering pressures between the ranges of 200 to 700MPa have been used by most of the researchers.

Iron-based BMG was fabricated by Lee et al [62]. Starting MG powders composed of Fe, B, Nb and Y were produced by atomization and fabricated into bulk using SPS processing. Powder samples placed in WC die was sintered at the Tg (873K) at a high pressure of 600 MPa. Amorphous fully densified (99.5%) compact was obtained. Magnetic properties of the sintered material was analyzed, and it was reported that saturation magnetization was enhanced when compared to the as-received powders [62].

Neamtu et al. [37] sintered Fe–based ($Fe_{75}Si_{20}B_5$) powders produced via mechanical alloying using SPS processing. Sintered samples were studied for their soft magnetic properties. Sintering temperature was varied (between 450 and 900°C), so was the dwell time (from 1 to 15 min), while the pressure was constant at 30MPa throughout the experiment. Boride phase $Fe_2B$ and silicide phase ($Fe_3Si$) was reported to crystallize during sintering at higher temperature. Good relative density and mechanical strength was also reported. It was finally reported that saturation induction and relative permeability increase with sintering temperature and time [37].

An iron based structural amorphous metal popularly called SAM 7 alloyed with Yttria was synthesized by SPS to determine its density and phase stability behavior [63]. The SAM 7–$Y_2O_3$ mixture, after ball milling was sintered at 600$^oC$ for 10min, and with the application of 30KN force, fully dense compacts with the evolution of only $Y_2O_3$ peaks were reported [63].

Microstructure and properties of iron based BMG with the composition $Fe_{48}Cr_{15}Mo_{14}Y_2C_{15}B_6$ was studied by Harimkar et al. [64]. This Fe–based BMG produced by high pressure gas atomization was fabricated by SPS at the $T_g$ and below. The applied uniaxial pressure, 350MPa, heating rate 150$^oC$/min were kept constant while dwell time was varied between 5 and 20min. It should be noted that powders were sintered in WC dies. Reports shows that highest densification (99%) was obtained at $T_g$, with however little crystalline peak belonging to $Fe_{23}(C, B)_6$. Densification was between 92 and 99% for sintering below $T_g$. It was finally reported that as sintering temperature increases, crystallite size increases leading to a drop in hardness at $T_g$ [64].

In order to obtain nanostructured alloys, MG precursors are usually sintered above their crystallization temperature, as crystallization is not expected below this temperature. The process of nanocrystallization involves phase separation, decomposition, and nucleation and growth of crystallites [65], and is also seen as a means to improve the properties of amorphous alloys. Crystallization products can be characterized using various techniques such as, scanning electron microscopy (SEM), Xray diffraction (XRD), and transmission electron microscopy (TEM), among others. Several studies to introduce nanoparticle into Fe-based amorphous phase has been achieved using several processes (laser processing, mechanical alloying, annealing and spark plasma sintering [46,65–70], however, this section will focus on spark plasma sintering process.

Ashish et al. [65] investigated the nanocrystallization of $Fe_{48}Cr_{15}Mo_{14}Y_2C_{15}B_6$ using small angle neutron scattering technique [65]. In this work this Fe-based MG based alloy powders were consolidated by SPS technique.  Sintering was performed over a wide of temperature covering both above and below the Tx. Phase analysis confirmed the presence of nanocrystalline $(Fe,Cr)_{23}C_6$ phase [65]. SANs experiments were also used to understand the crystallization growth path [65].

Ravi et al. [71] in his study titled "spark plasma sintering of Fe-Cr-Mo-P-B-C-Si amorphous alloy" consolidated the said composition after it was mechanically milled [71]. As it has been said previously mechanical milling of crystalline powders is one of such techniques for developing amorphous alloys. The evolution of nanocrystalline $Fe_3C$ and

$(Fe,Cr,Mo)_7C_3$ were reported and confirmed using SEM, XRD, and TEM analysis [71]. As sintering temperature increases, hardness and relative density also increased [71].

All the above investigations confirm the ability of spark plasma sintering in producing bulk nanostructured materials form amorphous starting materials.

## 2.3.2 Microstructure and phase analysis

Different phases, resulting from the processing of Fe-based amorphous alloys have been reported. These phases which are shown in table 2.1 are formed independent of the processing technique. Most of these alloys usually consist of body cubic centered α-Fe, several carbides or boride phases.

Table 2.1. Different phases formed as a result of processing Fe-Cr-Mo based alloys

| Alloy system | Processing | Phases | Ref. |
|---|---|---|---|
| Fe48Cr15Mo14Y2C15B6 | SPS | (Fe,Cr)23C6 | [68] |
| Fe70Cr15Mo4P5B4C1Si1 (wt. %) | SPS | α-Fe, Fe3C, M7C3 | [74] |
| Fe52Cr18Mo7B16C4Nb3 | Annealing | α-Fe, Fe3B | [69] |
| Fe48Cr15Mo14Y2C15B6 | Laser treatment | M23(C,B)6, M7C3 | [47] |
| Fe56Cr13Mo1.9B16.6P7.2C3.7Si1.6 (at.%) | Mechanical milling | α-Fe(Cr), Fe23(C,B)6, Fe3B, FeB, Fe2P | [70] |
| Fe52.3Mn2Cr19Mo2.5W1.7B16C4Si2.5 | Annealing | α -Fe, Fe3B, Fe23C6 | [72] |
| Fe43Cr16Mo16C15B10 | Annealing | α-Fe, M23(C,B)6, (Fe, Cr, Mo)7C3 | [73] |
| Fe43Cr16Mo16C15B10 | Laser melting and HVOF | α-Fe, Mo2(Fe,Cr)B2, (Fe,Cr)3Mo3(C,B), M23(C,B)6 | [74] |

## 2.4 Tribology

### 2.4.1 Tribology of amorphous and nanocrystalline Fe-based alloys

Immense studies have been done and reported for the tribological behavior of materials developed from Fe-based amorphous powders. A larger percentage of these investigations involving the deposition of MG powders as coatings [14,20,21,75–79] on metallic substrate have been observed. Fewer works have been observed for bulk amorphous alloys, and bulk crystalline alloys developed from amorphous precursors [22,23,80–82]. This section will discuss the various findings that cut across the Fe-based amorphous and crystalline alloys.

Jiang et al. [21] developed a FeCr7.3P6.34 C3.84Mo3.4Si2.41B0.82 wt.% amorphous powder from gas atomization process. These powders were thermally sprayed on steel substrates at room temperature. The coatings were further heat treated below and above the crystallization temperature to yield nanocrystalline coatings. Using a tribometer in a pin-on-disk mode, the wear performance of as sprayed amorphous coatings, as well as crystalline coatings was compared [21]. Figure 2.5 summarizes the findings from their investigations. Samples heat treated just above the crystallization temperature showed highest hardness as well as superior wear resistance. This was attributed to the formation of nanocrystalline phases developed as a result of temperature effect. The crystallization brings about strengthened fine grains that inhibit the free movement of dislocation during wear test [21].

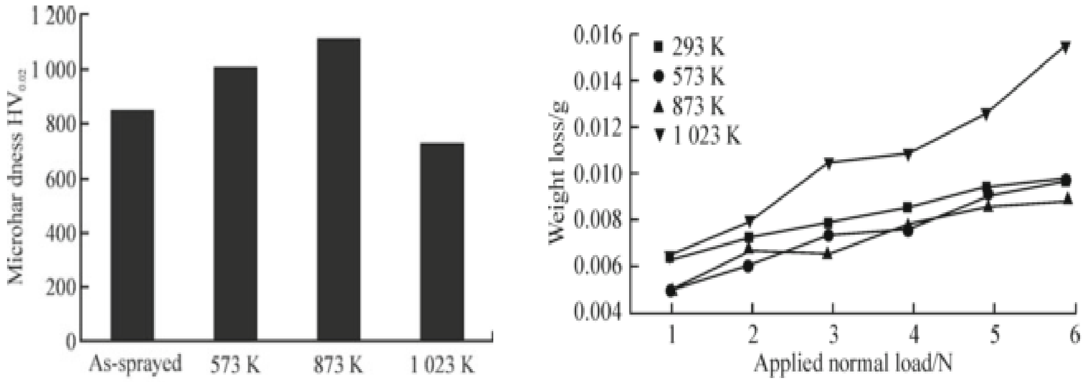

Figure 2.5. Hardness and weight loss of as-deposited and heat treated Fe-based coatings [21]

Dawit et al. [82] developed a Fe-based BMG by a copper mold conventional casting technique. The friction and wear behavior of the as-cast and annealed samples were investigated using a ball-on disk equipment. It was found the friction coefficient and wear loss of the as-cast amorphous alloy was lower and better that that of conventional steel samples [82]. Furthermore, it was reported that the BMG alloy was crystallized after annealing at 600 °C, and had a higher hardness but a lower wear resistance when compared to the as-cast BMG material [82].

Singh et al. [23] studied the effect of devitrification on the wear performance of iron-based Fe48Cr15Mo14Y2C15B6 (at.%) alloy. The Fe-based alloy powders, developed from high pressure gas atomization technique was fabricated into bulk sample using spark plasma sintering process, and further heat treated far above the temperature of crystallization. As-sintered samples were reported to be amorphous while annealed were partially crystalline [23]. The tribological performance of these materials were investigated under a ball-ondisc friction test mode. Coefficient of friction increased from 0.5 for the amorphous sample to about 0.6 for the annealed samples. As shown in figure 2.6, the annealed samples had a better wear performance when compared to the amorphous alloy due to their higher hardness and the nucleated carbide phases [23].

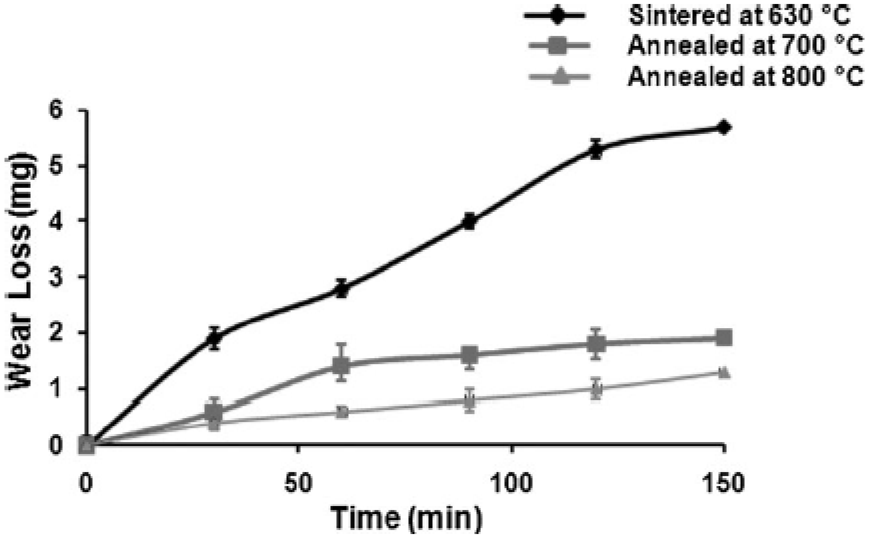

Figure 2.6. Wear loss of the sintered and annealed with respect to sliding time [23]

Maddala et al. [80] studied the sliding wear behavior of Fe50-XCr15Mo14ErXC15B6 (x=0, 1, 2 at%) alloy fabricated from a suction casting technique. Sample with 2 % Er was annealed for 10 and 100 minutes. The sample annealed for 100 minutes was reported to be crystallized, that at 10 minutes was structurally relaxed, while other samples remained amorphous. For all samples, it was reported that the crystallized sample exhibited the highest hardness, however it had the poorest wear resistance [80]. Furthermore the structurally relaxed sample whose hardness was just below the crystalline sample had the highest resistance to sliding wear [80].

# CHAPTER 3

# OBJECTIVES

To sum up the findings from the literature review, several works have been done on iron-based MG powders, ranging from depositing them as coatings on metallic substrates, fabrication of bulk amorphous materials, and investigating several of their properties and performance. However, few works been published in the area of developing nanocrystalline bulk materials from iron-based MG powder. In addition, the tribological performance of a nanocrystalline alloys developed from MG precursors has rarely been invstigated.

The aim of this research is therefore to understand the effect of sintering temperature on the microstructure and tribological performance of Fe-Cr-Mo-based bulk alloy consolidated by SPS. This knowledge is important in understanding the processing-property-performance relationship of this alloy. The proposed specific objectives of this study are:

- To study the effect of SPS sintering temperature on the densification, microstructure, phase evolution, and hardness of spark plasma sintered Fe–based MG powders.
- To investigate the tribological behavior and performance of the selected sintered specimens by SPS and compare it with conventional alloys.

# CHAPTER 4

# EXPERIMENTAL METHODOLOGIES

## 4.1 Materials (Iron based metallic glass material)

Iron-based metallic glassy powder having a nominal composition of $Fe_{52.6}Cr_{26}Mo_{17}C_{2.3}B_{2.1}$ (wt. %) was used for this investigation. The mean diameter of the powder particles was approximately 31 µm. This powder was prepared and supplied by LiquidMetal Technologies, USA. The metallic glass powders were prepared by high pressure gas atomization process. This process involves melting a mixture of Fe, Cr, Mo, B and C elemental powders under a high purity argon atmosphere after which the liquid melt is rapidly atomized using high purity inert gas.

## 4.2 Materials Processing

### 4.2.1 Spark Plasma Sintering

Spark Plasma Sintering equipment type HP D 5, manufactured by FCT systeme GmbH, is used to consolidate the amorphous samples. This equipment is shown in figure 4.1. The SPS equipment used consists of the heating chamber, cooling unit, pump and a computer unit. This equipment is capable of reaching high temperatures and high heating rate, but in this study, a maximum temperature and heating rate of 1000 $^{o}$C and 100 °C/min, respectively was used. Sintering was done under a vacuum of 0.75 Torr to achieve high purity in sintered samples. Using graphite dies and punches, fabrication was done due to equipment restriction at a limited pressure of 50 MPa for samples having a diameter of 20 mm and a thickness of about 5 mm. To accurately measure the sintering temperatures, a thermocouple was placed in the die. Sample fabrication is achieved by lining the dies and punches with a graphite sheet. This lining also facilitates the easy removal of samples after sintering. After lining, 10 g of the iron based powders were weighed and poured into the die and placed in the heating chamber of the SPS equipment. Temperature, pressure and heating rate of interest was imputed from the computer. The as received powders were fabricated at 500, 600, 700, 800, 900 and 1000 $^{o}$C.

Figure 4.1. The spark plasma sintering equipment used in this work

### 4.2.2 Density Measurements

Densification measurement were done by measuring the density of the sintered sample and dividing by the theoretical density. The density of the sintered samples was measured using a Mettler Toledo kit. With this kit, and following the Archimedes principle, the sample weight is measured both in air and distilled water after which the equation below is used to estimate the experimental density.

$$\rho = \left(\frac{A}{A-B}\right)(\rho_o - \rho_a) + \rho_a \qquad \text{Equation 4-1}$$

Where

$\rho$ = Density of sintered sample (Experimental density) in g/cm$^3$

A = weight of sintered sample in air

B = weight of sintered sample in distilled water

$\rho_o$ = density of distilled water

$\rho_a$ = density of air

Theoretical density of the Fe-based alloy is 7.87 g/cm$^3$

$$Relative\ density\ (\%) = \frac{Experimental\ density}{Theoretical\ density} \qquad \text{Equation 4-2}$$

## 4.3 Characterization

### 4.3.1 Microstructure Analysis

The morphology and particle size of the powdered alloy was measured using the scanning electron microscope (SEM). Micrographs were obtained from the both SEM and FE-SEM equipment. The maximum, minimum, and average particle size was determined. Low and high magnification images were taken to check the presence of open and closed pores. The precise average particle size of the powders was further ascertained using the particle-size analyzer (Microtrac model S3500/Turbotrac).

For microstructural analysis of sintered samples, a small section of the bulk alloy was cut and mounted in epoxy. The samples were then ground to in a stepwise order, starting with rough 240 grit, followed by 320, 400 and lastly fine 600 grit SiC papers. After this, the finely ground samples were polished using diamond suspension starting with 9 µm, 6 µm, 3 µm, and then 1 µm. The sample were finally polished using alumina suspension of 0.3 µm size. A field emission scanning electron microscope (FE-SEM) (Tescan Lyra-3) (shown in figure 4.2) was used to analyze the morphology of the finely polished cross section surfaces of the sintered compacts. Secondary electron (SE) and back scattered electron (BSE) images at low and high magnifications were taken. Energy dispersive spectroscopy was used to analyze the composition of the phases.

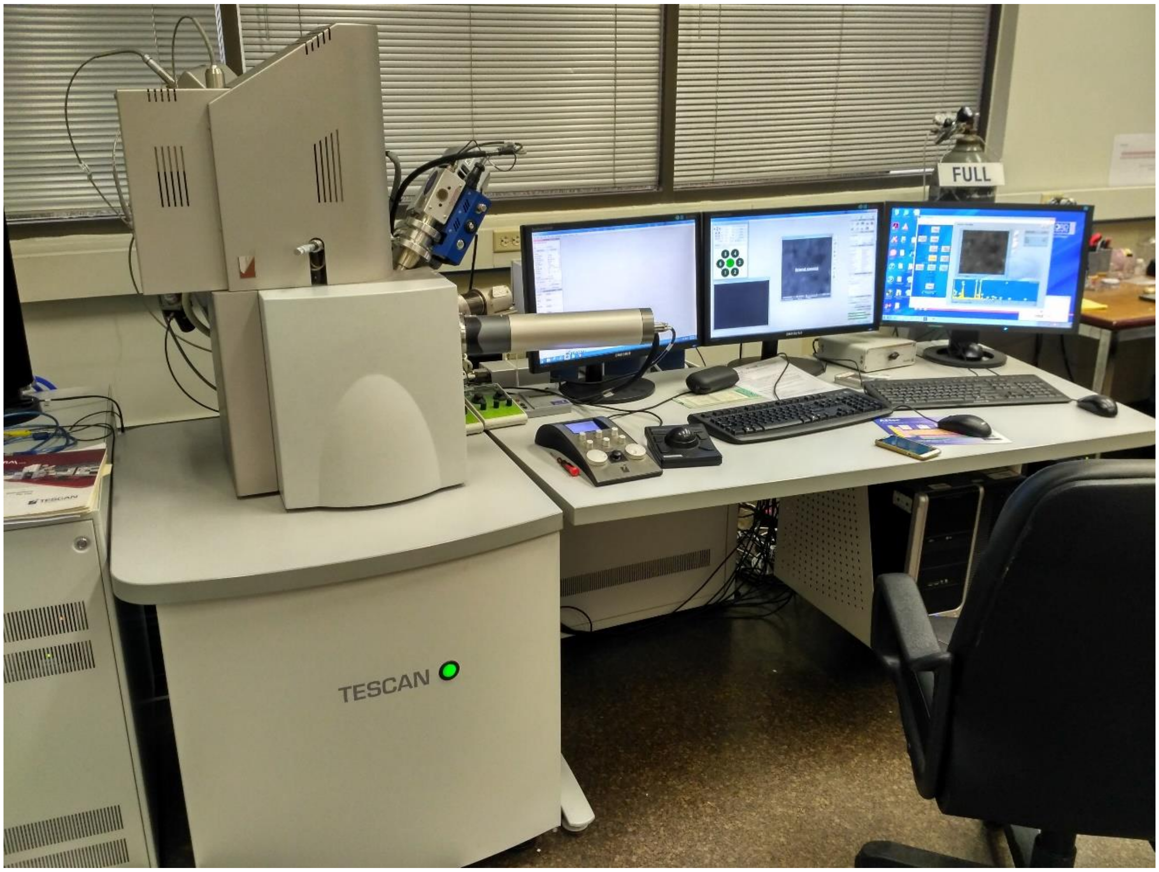

Figure 4.2. Field emission scanning electron microscope

### 4.3.2 Phase Analysis

The transition temperatures, (i.e. glass transition, crystallization temperature, and melting temperatures) of these powders were measured using the differential scanning calorimetry (DSC) equipment. The powder was placed in an alumina pan and was analyzed in an Argon environment within a temperature ranging from 30 to 1400 °C under a 10 K/min constant heating rate.

X-ray diffractometer (XRD) as shown in figure 4.3 was used to understand the structure of the as-received powder and structural changes that may have occurred as a result of spark plasma sintering. A Rigaku Ultima IV X-ray diffractometer was used. The materials to be examined were placed in the XRD chamber and operated with a Cu Kα radiation source with a wavelength of 1.5406 Å. The equipment was operated at 40 kV and 40 mA, while scanning operation was done at 0.02°/s for 1 s/step over a 2-theta value 30 to 90°. These conditions for which most of the peaks should be captured, and for which an XRD pattern with high signal to noise ratio should be obtained were chosen based on literature.Data was recorded using the PDXL software. Peak evolution were matched from the software and with peak database.

Figure 4.3. X-ray diffraction equipment

### 4.3.3 Microhardness

Hardness measurements for all samples investigated were made using a Vickers microhardness tester (MMT-3 digital microhardness tester, Buehler). Applying a load of 300 gF (2.94 N) for a holding time of about 9 s, approximately 15 indentations from different areas of the polished samples were taken, and the average of these results is reported.

## 4.4 Sliding Friction and Wear Tests

For all samples, an unlubricated sliding wear test was performed using a UMT-3MT tribometer (Bruker, Campbell, CA) tribometer in a ball-on-disk configuration. Due to the size of the sintered sample, and the nature of the tribometer sample holder, the samples were initially mounted in epoxy. They were ground, polished, and finally rinsed with acetone. The sintered samples were tested at a speed of 0.05 m/s, and under a load of 5 N. Stainless steel and alumina counterface were used to create a wear track of 4 mm diameter on the sintered sample, as well as other disk samples (D2 tool steel and carbon steel). The cross sectional area of the worn tracks were measured using an optical profilometer after which the obtained value was used to obtain the wear volume. Images of the tribometer and optical profilometer is presented in figure 4.4 and 4.5 respectively. The wear volume of the stainless steel and alumina counterface materials were measured based on the ASTM G99 [83] standard by measuring the average scar diameter. The formula from the standard is presented in equations 4-3 and 4-4. For microstructural studies, a SEM equipped with an EDS detector was used to analyze the worn surfaces in order to predict the probable wear mechanism.

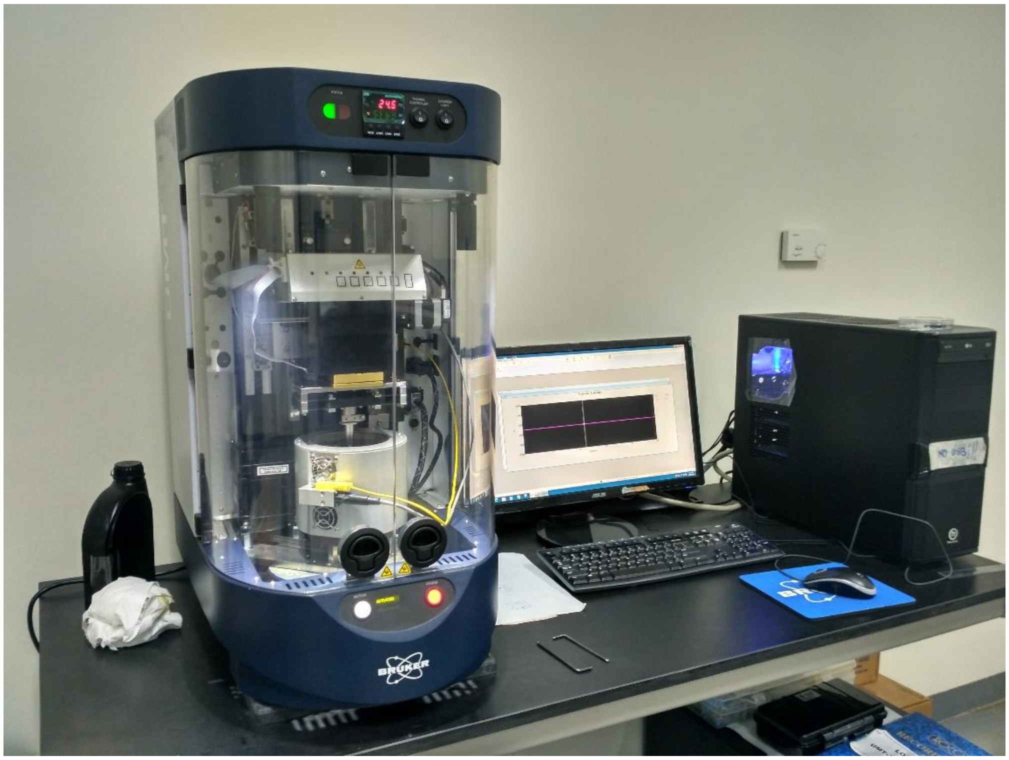

Figure 4.4. The UMT tribometer

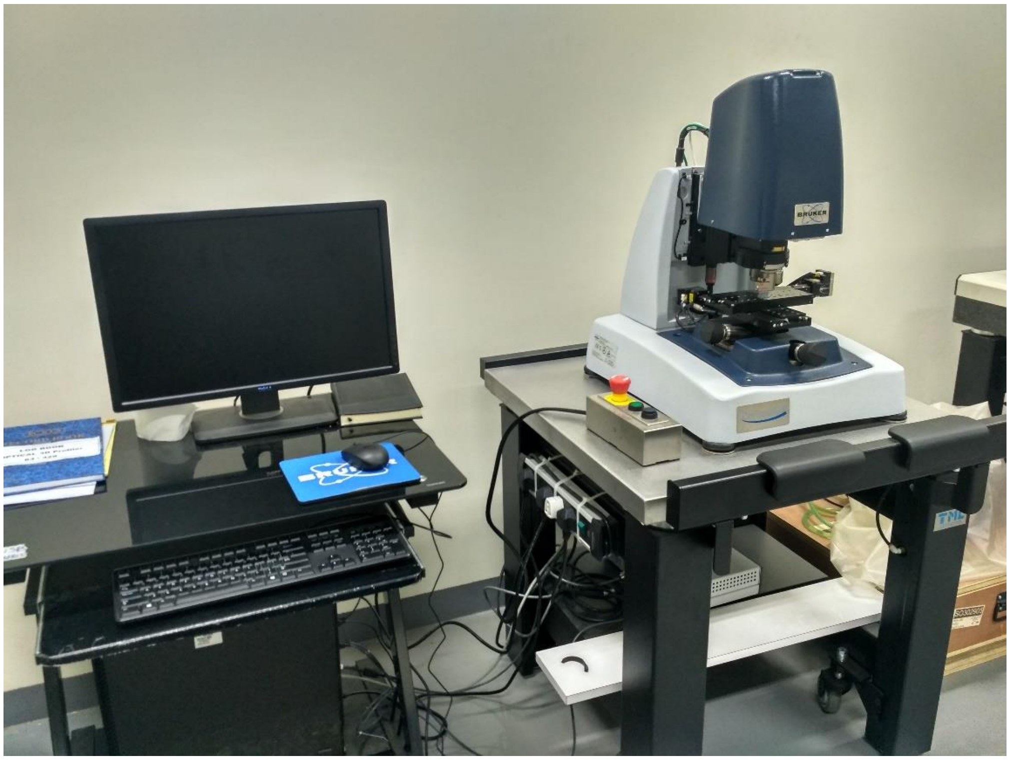

Figure 4.5. The optical profilometer

$$Ball\ volume\ loss = \left(\frac{\pi h}{6}\right)\left[\frac{3d^2}{4} + h^2\right] \qquad \text{Equation 4-3}$$

Where ‘h’ is the height of material lost, and is given by;

$$h = r - \left[r^2 - \frac{d^2}{4}\right]^{\frac{1}{2}} \qquad \text{Equation 4-4}$$

Where d = diameter of the wear scar, and

r = radius of the counterface

# CHAPTER 5

# RESULTS AND DISCUSSION

## 5.1 Introduction

Comprehensive discussions that supports the results obtained during the course of this research is presented in this chapter. Results of the densification behavior, microstructure and phase evolution of the Fe-Cr-Mo–based alloy fabricated by SPS are presented and discussed. Here, we discuss in the detail the results from the initial powder characterization, followed by the effect of sintering temperature on densification behavior, microstructure and phase evolution. DSC, XRD and FE-SEM techniques were used during the densification and microstructural investigation of the sintered alloy. Furthermore, results from sliding wear tests explaining the tribological behavior of the most dense alloy, compared with standard steel samples is presented.

## 5.2 Densification and Microstructure of sintered Fe-Cr-Mo–based alloy

Due to the ability of the spark plasma sintering technique in developing bulk metallic glass, nanocrystalline and fully crystalline materials from amorphous precursors, the Fe-Cr-Mo–based metallic glass powders was fabricated using this processing technique. The densification and hardness was studied. Furthermore, the effect of temperature on the evolution of crystalline phases was studied.

### 5.2.1 Powder characterization

Fig. 5.1 shows the DSC results for the as-received Fe-Cr-Mo-based alloy powder. The powder exhibited an exothermic peak corresponding to the glass transition temperature (Tg) at 602°C, followed by an exothermic peak corresponding to the crystallization temperature (Tx) at 645°C. The melting temperature (Tm) of the powder was measured at 1150°C. Similar trends have been reported for Fe-based MG alloys ($Fe_{50}Ni_{30}P_{13}C_7$) [84]. Based on these transition temperatures, the sintering temperatures have been selected.

Fig. 5.2 presents the XRD pattern obtained from the gas-atomized starting powder. It shows a broad diffraction peak, which is a characteristic of a completely amorphous (or glass) structure. Thus, it confirms the glassy structure of the powder. Fig. 5.3a presents the SEM morphology of the as-received powder. The powder particles have a spherical shape with a smooth surface, which is a characteristic of powders prepared by the gas atomization process. Particle size analysis (Fig. 5.3b) showed that the mean diameter of the powder particles was approximately 31 ± 14 µm.

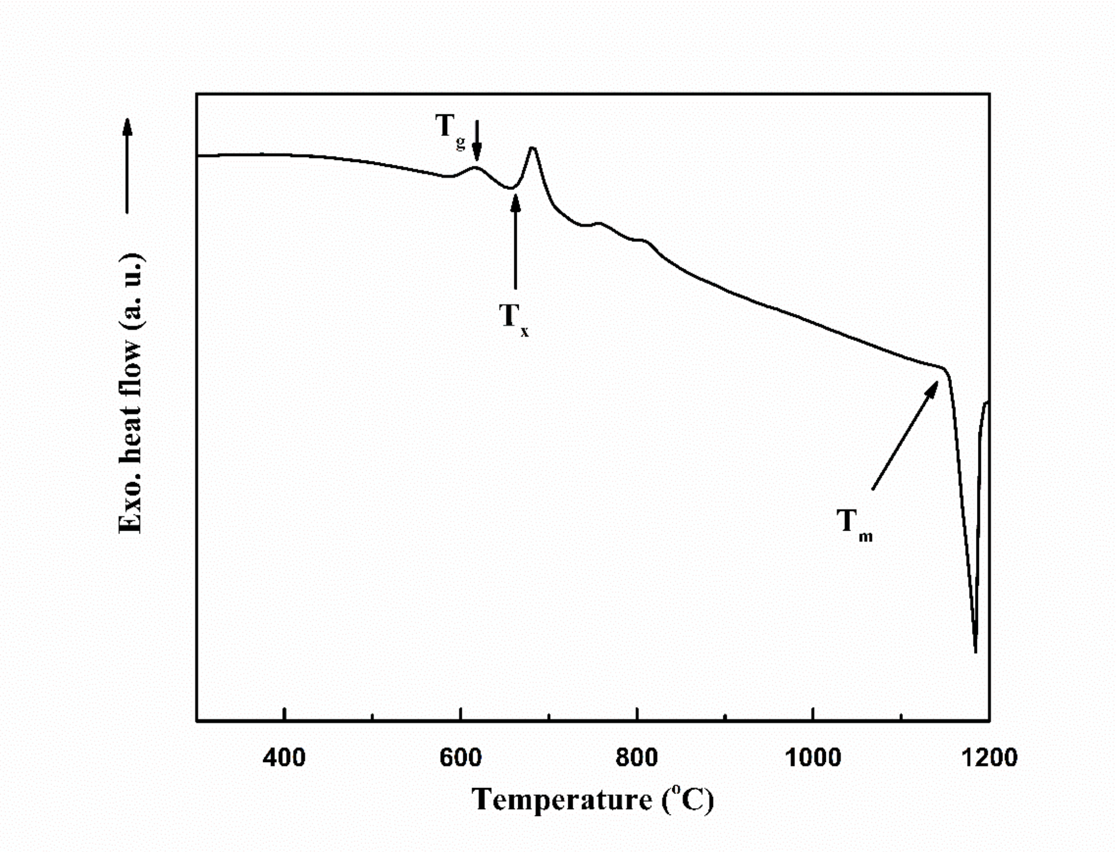

Figure 5.1. DSC result of the as-received Fe-Cr-Mo-based alloy powder.

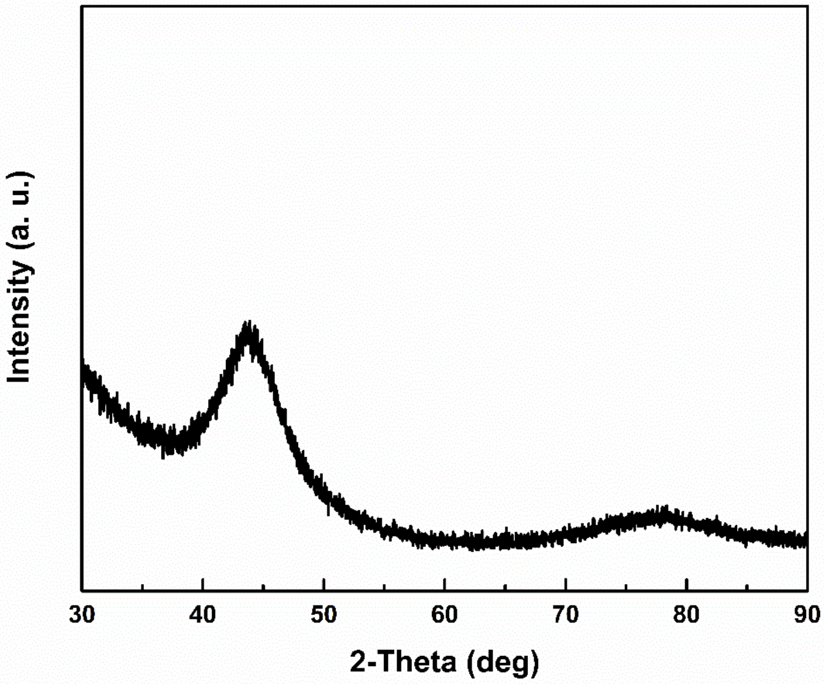

Figure 5.2. XRD pattern of the amorphous as-received Fe-Cr-Mo-based alloy powder.

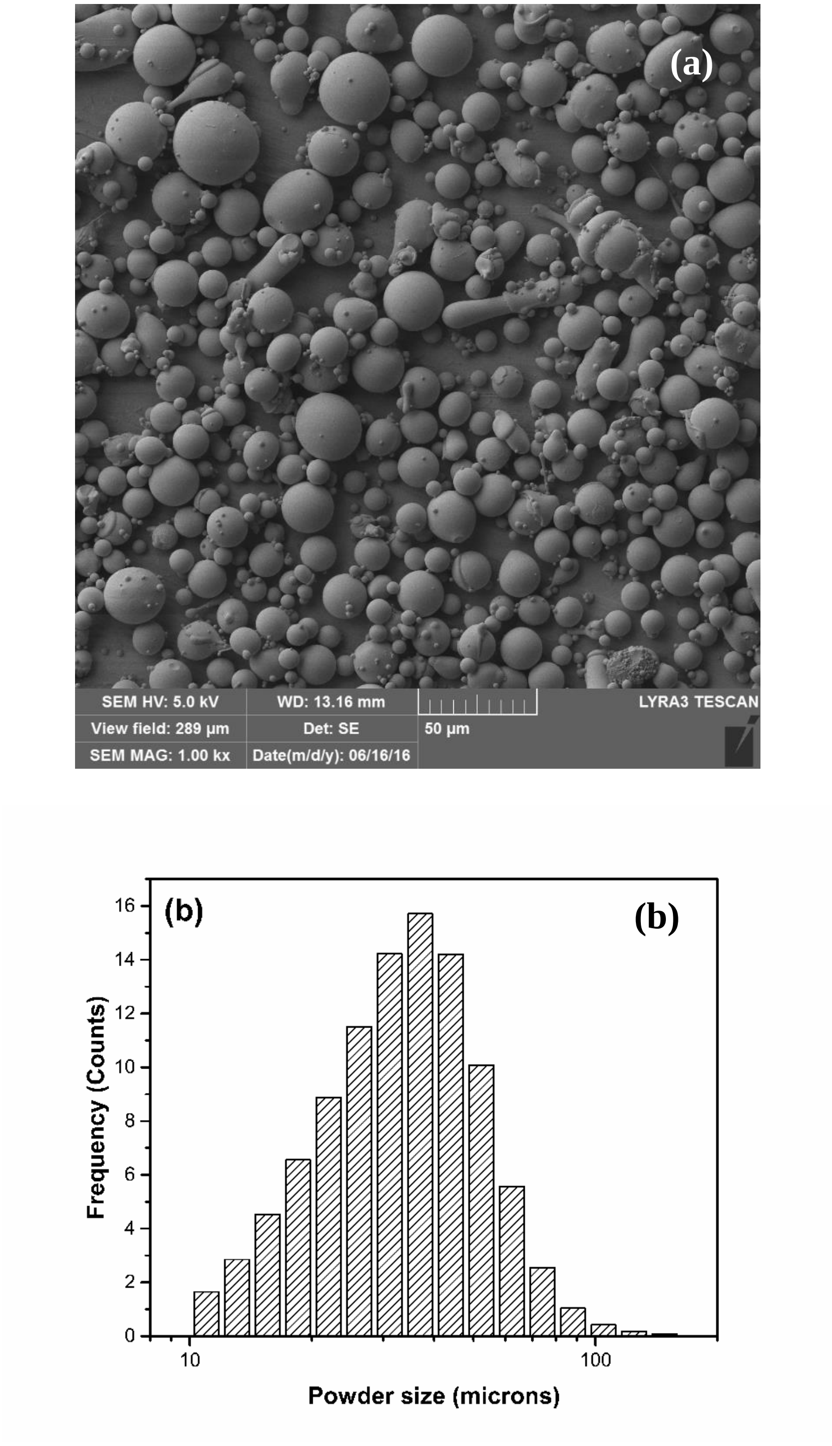

Figure 5.3. (a) SEM micrograph of the as-received Fe-Cr-Mo-based alloy powder; (b) Particle size analysis of powder particles.

### 5.2.2 Densification

The powder was consolidated by SPS at different temperatures. The effect of sintering temperatures on the sample density is presented in Fig. 5.4. The relative density increases with increase in the sintering temperature. However, the samples sintered at 900 and 1000 °C have the same density. Similar densification trends have been reported for similar alloys [71,85]. The samples sintered at temperatures close to the crystallization temperature, $T_x$, (645°C) have a densification of less than 84%. However, in previous reports [63,64], Fe-based amorphous alloys were consolidated at $T_x$, and a greater densification was obtained. Notably, the compositions of the alloys investigated in these previous reports differed from that of the alloy investigated in the present study. Furthermore, the sintering was performed at higher pressures (between 100 and 200 MPa) than that used in the present work (50 MPa).

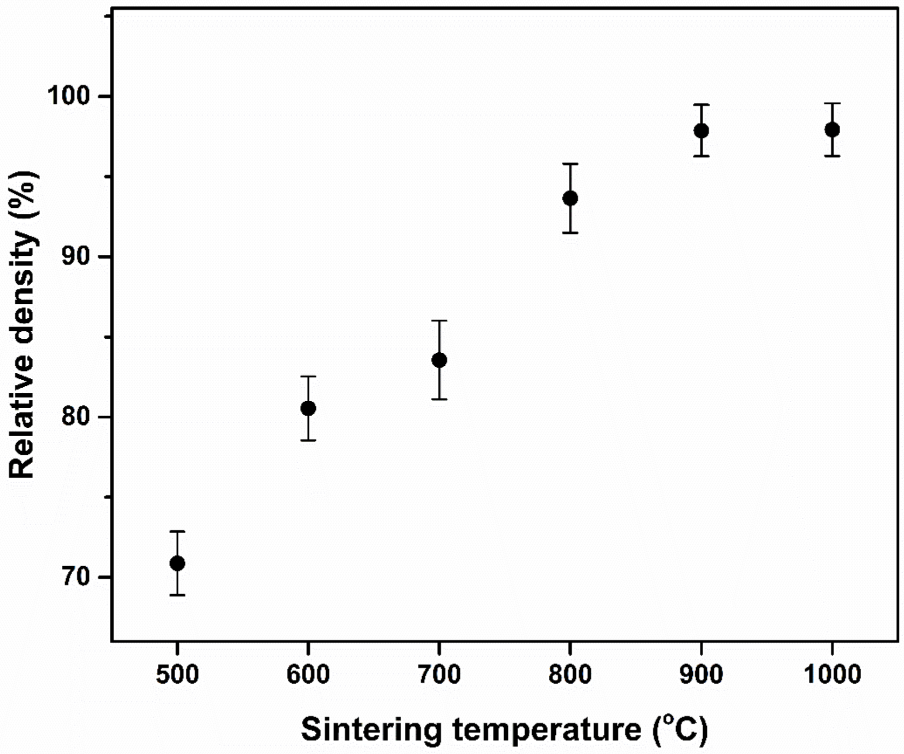

Figure 5.4. Densification results for the samples sintered at various temperatures.

For sintering temperatures starting from 500 to 700 °C, the relative density of the sintered samples increases gradually up to 83.6%, after which a sharp increase to about 93.6% was noted for the bulk sample at 800 °C. The samples sintered at 800, 900 and 1000 °C exhibited better densification with increasing sintering temperature, reaching a maximum value of 98%. The increasing sintering temperature is, therefore, responsible for the improved densification, and this is due to the elimination of pores, increased necking and enhancement in the bonding between powder particles.

### 5.2.3 Microstructure analysis of the sintered samples

Microstructure analysis has been carried out to understand the effect of sintering temperature on microstructure and development of crystal particles. Fig. 5.5 shows the XRD results for the samples sintered at different temperatures. Sintering at temperatures below the crystallization temperature ($T_x$ = 645 °C) led to the evolution of a few crystalline peaks, i.e., the background of the pattern was the pattern of an entirely amorphous sample, with just a few new crystalline peaks. Thus, the almost completely amorphous structure of the starting powder was retained at these temperatures. The reasons for these minor crystallization that occurred below the Tx could be as a result of overheating that occurs in the region near the surfaces of the powder particles during sintering [16].

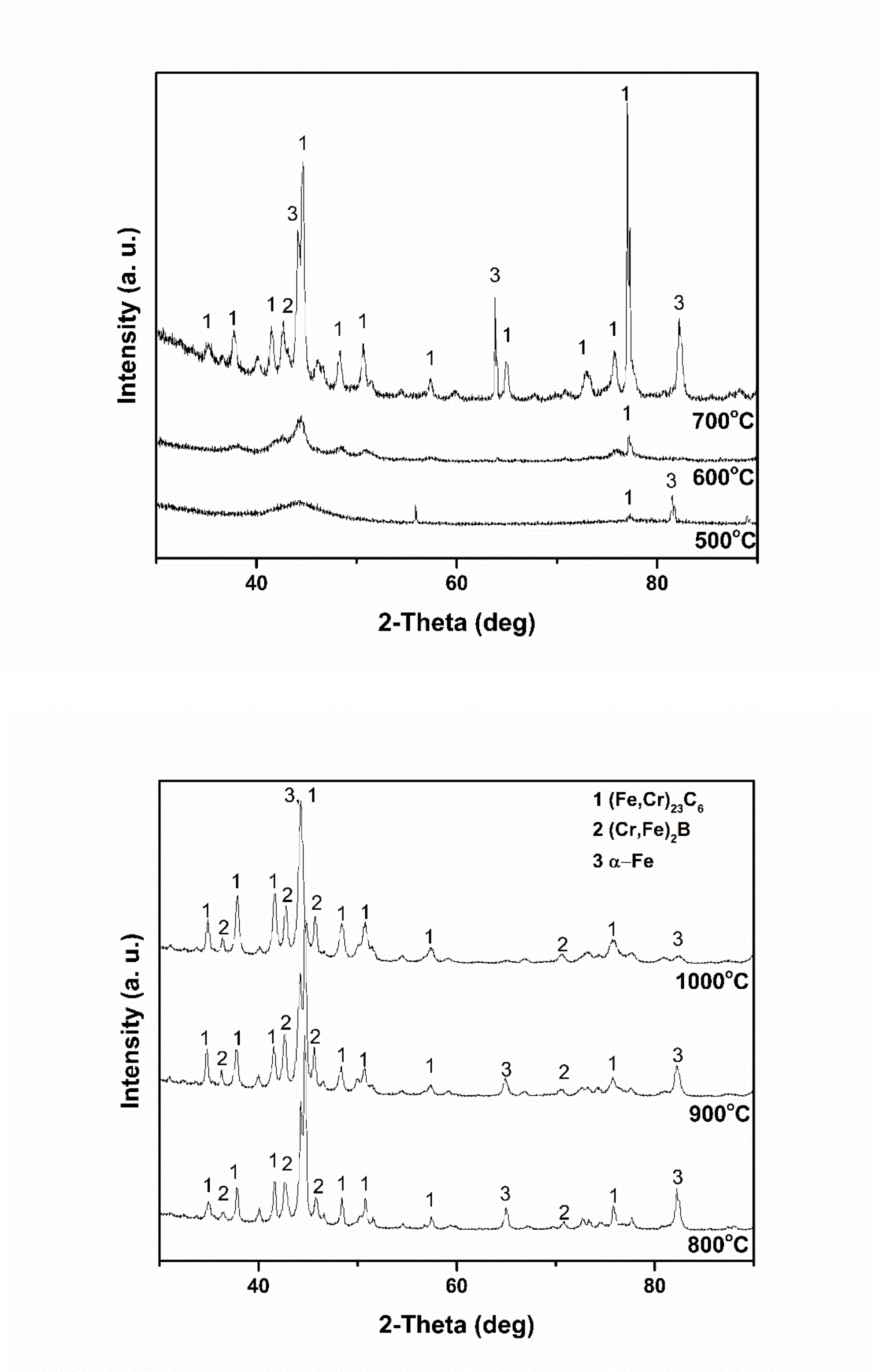

Figure 5.5. XRD results for the SPS sintered samples at different temperatures.

As temperature increases above 700 °C, the intensity of crystalline peak increases which indicates enhanced crystallization and the formation of crystalline phases. This composite consists of the BCC α-Fe (ICDD # 03-065-4899) [86], and $M_{23}C_6$ phases as well as a small amount of $M_2B$ (with hexagonal crystal system), where M represents Fe, Cr and Mo. The $M_{23}C_6$ crystalline phase belongs to a cubic crystal system, space group: Fm-3 m (225) [65].

Fig. 5.6 presents the SEM images of the sintered alloy showing the nanocrystalline particles formed as a result of temperature influence during SPS. It is evident from the microstructure of the sample sintered at 800 $^{o}$C (Fig. 5.6a), that the sample was not fully sintered as observed from the incomplete necking and presence of closed porosities in each particle (shown in the inset) as well as open porosities. As sintering temperature increases above 800 $^{o}$C, better densification was obtained, however, some closed porosities were noted.

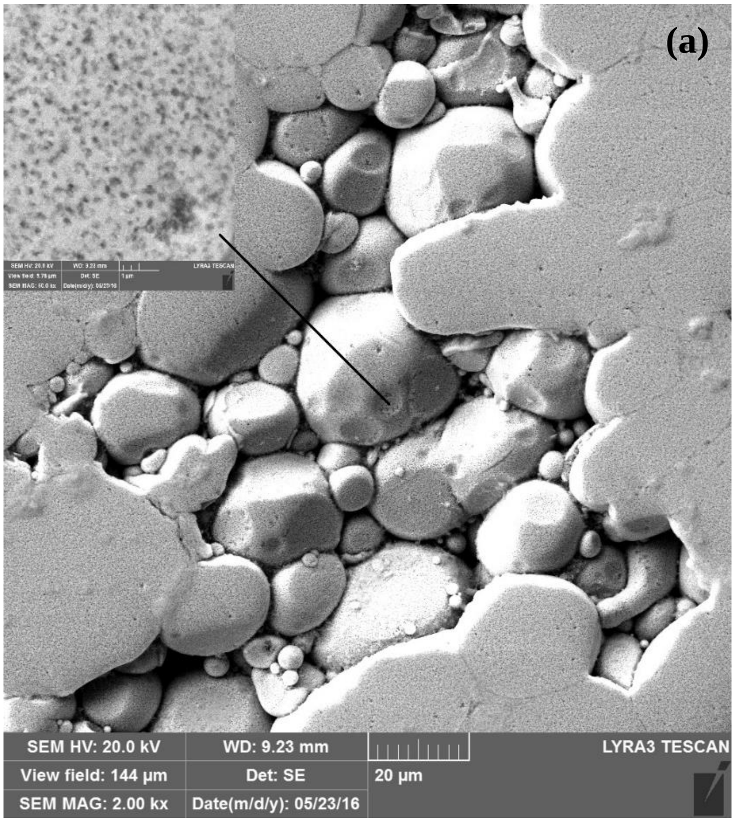
(a)
SEM HV: 20.0 kV
WD: 9.23 mm
LYRA3 TESCAN
View field: 144 µm
Det: SE
20 µm
SEM MAG: 2.00 kx
Date(m/d/y): 05/23/16

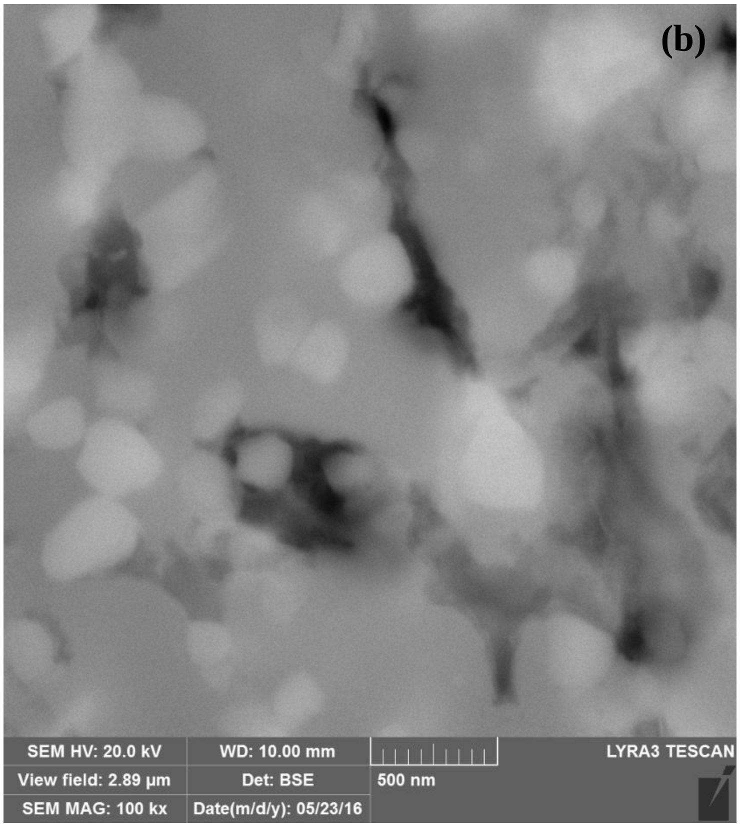
(b)
SEM HV: 20.0 kV
WD: 10.00 mm
LYRA3 TESCAN
View field: 2.89 µm
Det: BSE
500 nm
SEM MAG: 100 kx
Date(m/d/y): 05/23/16

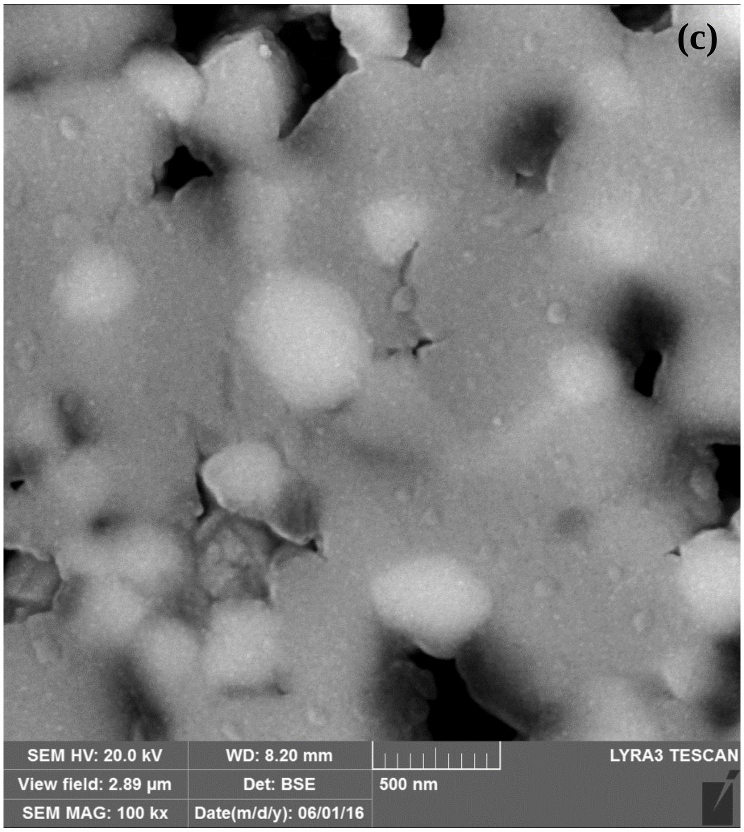

Figure 5.6. SEM images of specimens sintered at (a) 800 °C, (b) 900 °C and (c) 1000 °C.

Figure 5.6b and c shows the microstructure of the sintered alloys at 900 and 1000 $^{o}$C. As observed from the EDS analysis plot (Fig. 5.7), the gray or darker particles in the BSE microstructural images of both samples are rich in C, and therefore indicates a  metallic carbide phase ($M_{23}C_6$) [74], while the brighter particles (rich in B) represented metallic boride ($M_2B$). The $M_{23}C_6$ as clearly seen from the sintered samples had its particles in the micrometer size range. However, the boride particles for the samples sintered at 900 and 1000 $^{o}$C, had an average particle size around 110–360 nm. The evolution of crystalline phases from amorphous structure presents a possibility of understanding the kinetics and micromechanisms of crystallization. Furthermore, due to the poor tensile ductility of BMGs, in-situ devitrification of the amorphous phases brings with it the possibility of improving the global plasticity of BMG alloys [16].

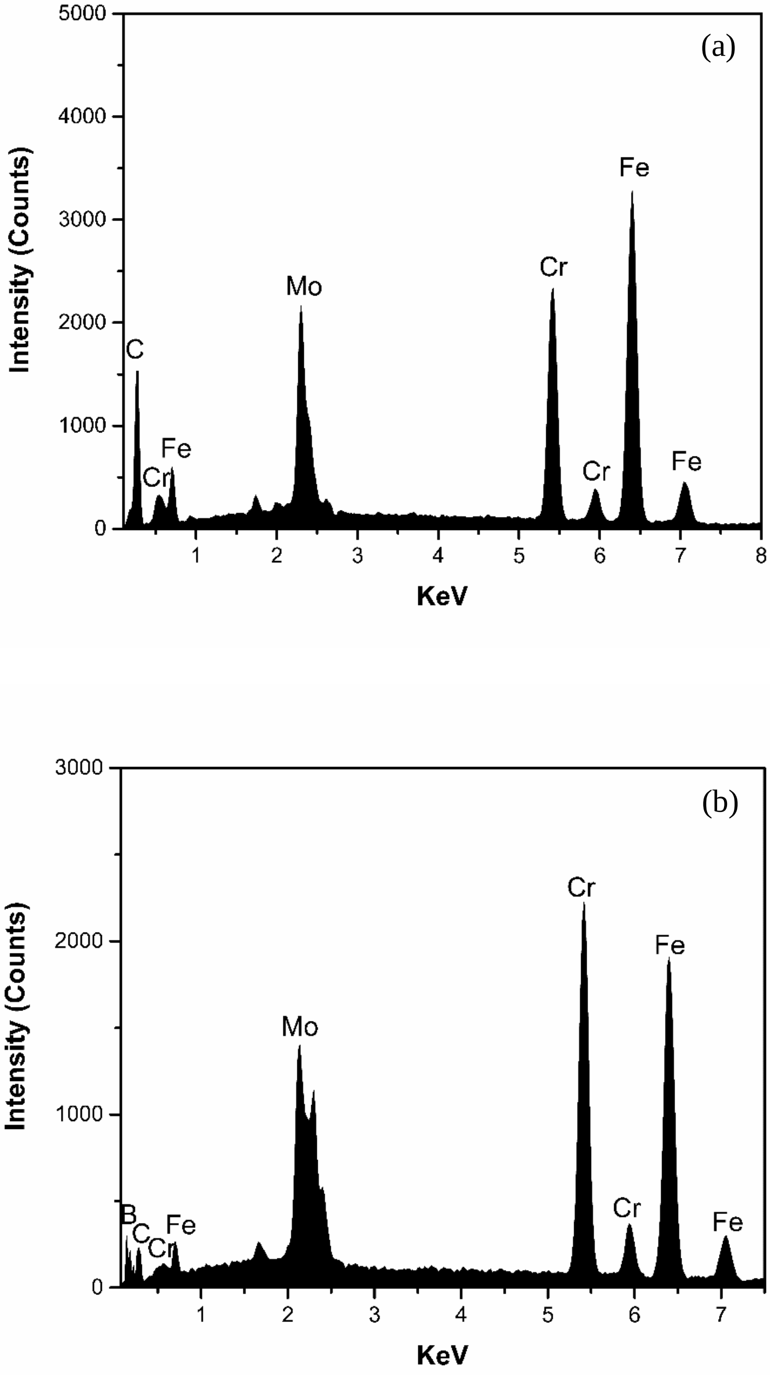

Figure 5.7. EDS analysis showing the formation of (a) carbide and (b) boride phases

### 5.2.4 Microhardness

Fig. 5.8 shows the Vickers microhardness trend for the samples sintered at 800, 900 and 1000 $^o$C. As a result of incomplete densification during the sintering of samples at temperatures below 800 $^o$C, microhardness values could not be evaluated. When sintering was performed at 800 $^o$C, the sintered sample exhibited a hardness of about 840 HV. A rapid enhancement in hardness was observed when the amorphous alloy was sintered at 900 and 1000 $^o$C. The hardness increases as the sintering temperature increases, which is a similitude to the trend in relative density. This, therefore, implies that densification during sintering plays an important role in the enhancement of hardness. Furthermore, higher crystallization (formation of nanocrystalline phases), and better bonding between the powder particles are important factors for the increase in hardness [47].

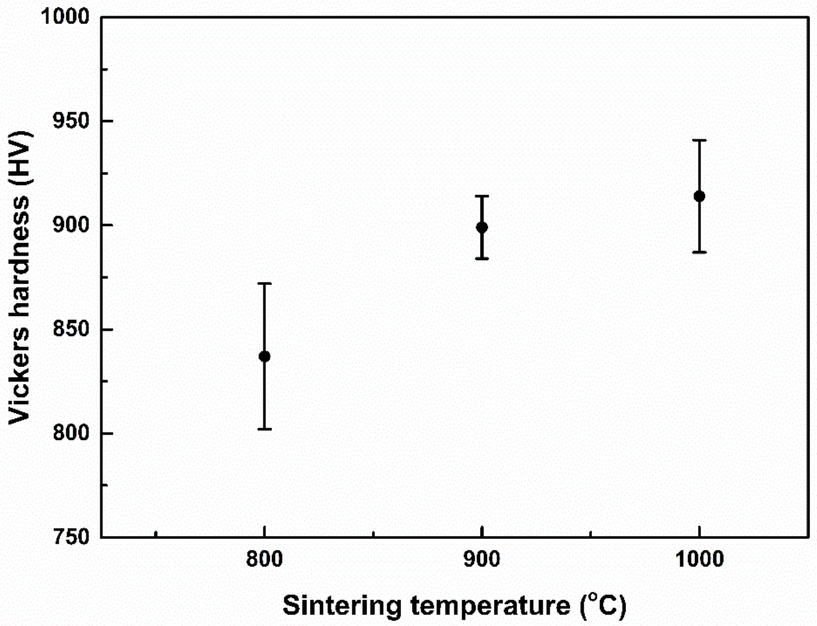

Figure 5.8. Vickers hardness of the samples sintered at various temperatures.

## 5.3 Tribological behavior of the sintered Fe-Cr-Mo–based alloy

The results from the study of the densification and microstructure of the bulk samples fabricated by spark plasma sintering was was presented in section 5.2. Based on this study, the sliding wear performance of the material with the best densification is studied. Results are therefore presented in this section. Different counterface materials were used to study the tribological properties of this material.

### 5.3.1 Microstructure and phase analysis

The SEM secondary electron micrograph of the amorphous powders, as well as that of the polished surface of the spark plasma sintered bulk alloy is presented in Figure 5.9. The micrograph of the powders (Fig. 5.9a) shows that the particles have a smooth surface and are spherical in shape, which is characteristic of materials produced via gas atomization route. Micrograph from the polished cross section of the sintered alloy (Fig. 5.9b) shows a microstructure with minimal porosities. The density of the specimen sintered at 900 $^{o}$C was measured using the Archimedes technique and the relative density is reported to be approximately 98%, and this shows that the sintered sample is applicable for microstructure and wear studies.

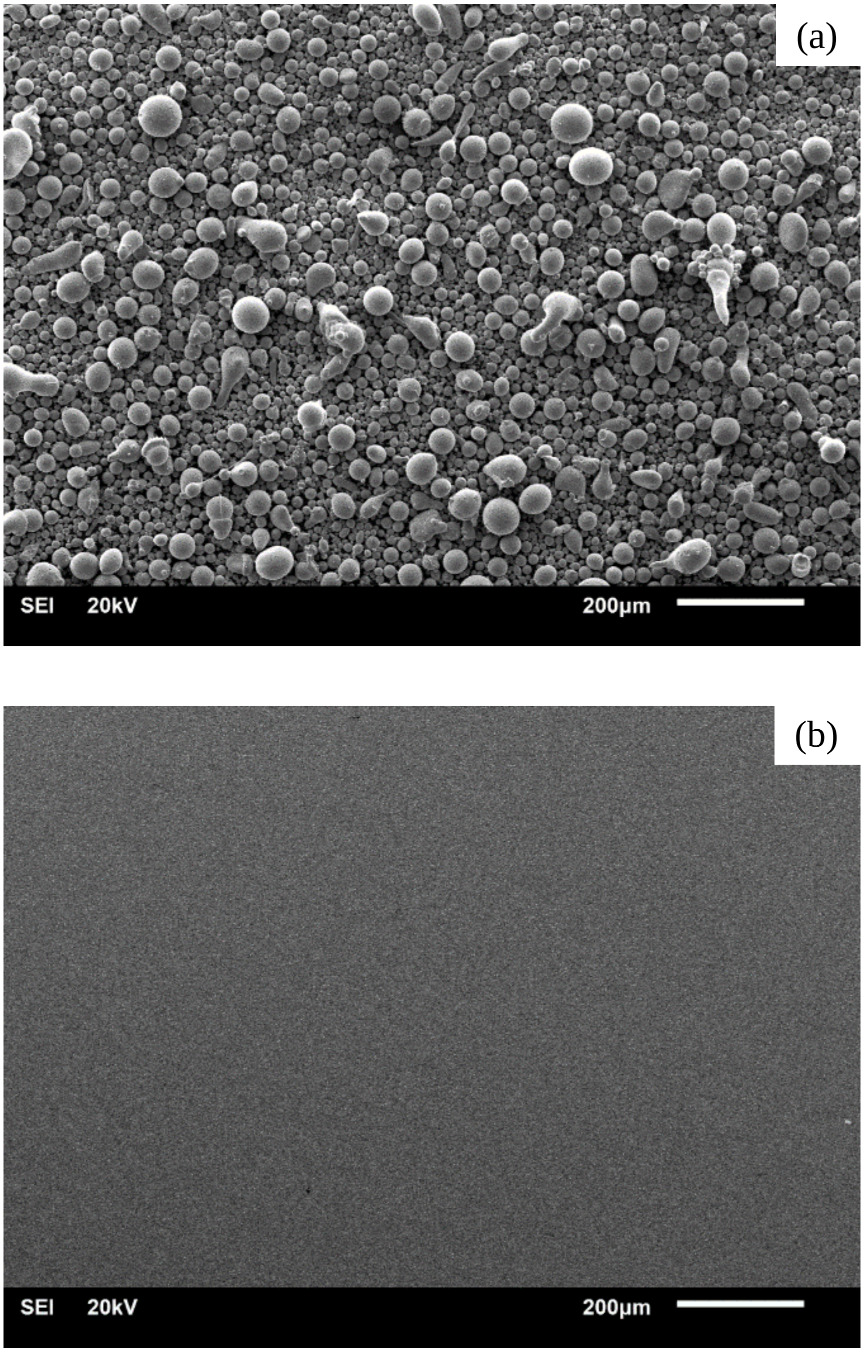

Figure 5.9. SEM micrographs of the Fe-Cr-Mo (a) as-received amorphous powder and (b) polished surface after SPS.

XRD results shown in Figure 5.10 confirms the glassy nature of the as received powders, as a result of the presence of a broad diffuse peak observed at a 2-theta value ranging between 40° and 47° similar to many iron-based amorphous alloys [74,87]. The evolution of sharp crystalline peaks upon sintering at 900 °C is also presented in Figure 5.10. Sharp peaks indicating a fully crystalline structure is seen from the XRD plot. The devitrification of the Fe-based sample brings about a sharp crystalline peaks belonging to body-centered cubic (BCC) α-Fe, $(Fe,Cr)_{23}C_6$, together with small amount of $(Cr,Fe)_2B$. The presence of these crystallization particles in the sintered alloy are often responsible for the enhanced hardness of these Fe-based alloys [46].

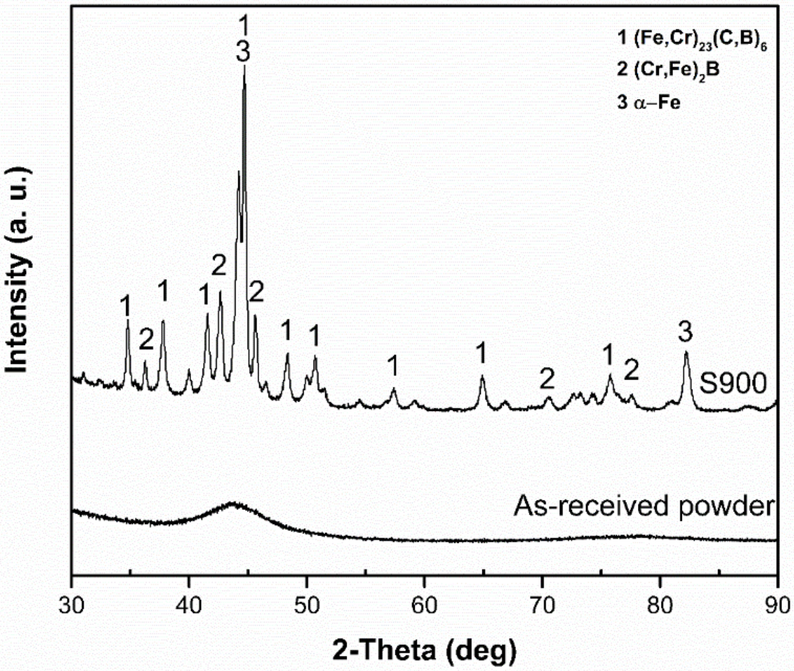

Figure 5.10. XRD pattern of the Fe- Cr-Mo powder and the sample sintered at 900 $^{o}$C. The amorphous character is observed from the powders. The crystalline peaks resulting from the spark plasma sintered bulk sample is also presented.

The backscattered electron micrograph from the sample sintered at 900 °C which confirms the presence of the crystalline phases is shown in Figure 5.11a. From the electron images, it is evident that the microstructure of the sample sintered from amorphous powders consists of bright and grey particles. The EDS elemental analysis (Figure 5.11b) of the grey particles confirms a Fe-rich phase consisting of Cr, Mo and C while the bright particles consists of a Cr-rich phase consisting of Fe, Mo and B. The bright phase which had a particle size of about 110–360 nm was within the range to be termed nanosized material as stated by Meyers et al. [28]. The XRD results of this bulk sample as shown in Figure 5.10 confirms that the grey phase gave peaks of iron and chromium carbide ($M_{23}C_6$), while peaks from the bright phase was chromium and iron boride ($M_2B$). For similar Fe-based sintered samples, both phases have been reported [23,88]. Obviously, the SPS of the Fe-based MG powders beyond the crystallization temperature results in the emergence of a bulk sample with nanocrystalline phases.

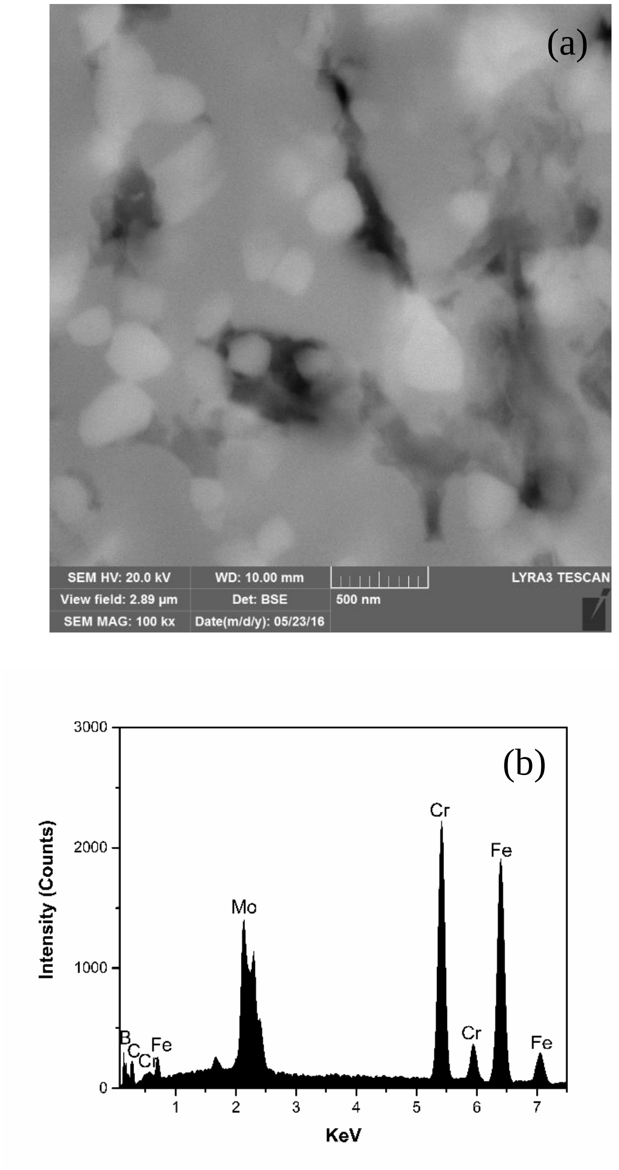

Figure 5.11. (a) SEM (BSE) micrograph and (b) EDS elemental analysis of the bright particles from the Fe-Cr-Mo-based sample sintered by SPS at 900 °C.

### 5.3.2 Microhardness

Vickers indentation measurements on a microscopic scale was performed to determine the hardness values of the slider and counterface materials. The sintered Fe-based alloy exhibited a bulk hardness of 899 ± 15 HV (8.8 ± 0.1 GPa) at an applied load of about 3 N. This value represents the hardness of all phases together with the interfaces between them, as it was difficult to single out each phase to measure their hardness. When compared with carbon steel and D2 tool steel, a lower microhardness values of 247 ± 15 HV for carbon steel and 871 ± 33 HV for D2 tool steel was experienced. The sintered-bulk alloy exhibited a higher hardness value. When the D2 tool steel was analyzed using SEM and EDS, the presence of only carbide particles were observed. The higher hardness of the sintered alloy may be due to the additional presence of boride particles as observed from their micrograph. Alloys similar in composition to the sintered Fe-based alloy have not been investigated. The summary of the hardness of all materials is presented in table 5.1.

Table 5.1. The hardness values (in HV) of the materials used in the investigation.

| | Materials | Hardness [HV/0.3] |
|---|---|---|
| Slider | Sintered sample | ~ 900 ± 15 |
| | D2 tool steel | ~ 871 ± 18 |
| | Carbon steel | ~ 247 ± 12 |
| Ball | Stainless steel | ~ 831 ± 14 |
| | Alumina | ~ 1723 ± 89 |

### 5.3.3 Sliding wear performance

Under unlubricated conditions, sliding wear tests were performed using both stainless steel and alumina counterfaces to obtain the coefficient of friction and wear rate. Figure 5.12a shows the plot of the COF as a function of sliding distance, under constant normal load of 5 N load and a sliding speed of 0.05 m/s, for the sintered alloy, carbon steel and D2 tool steel when slid against stainless steel counterface. The steady state COF of the sintered sample is almost similar to that of the tool steel during the wear test. However, during the early cycles of sliding (at about 8000 cycles), the sintered sample experienced a run-in period after which it stabilizes into the steady state sliding region. The average steady state COF of the Fe bulk alloy was 0.84 ± 0.04 while that of D2 tool steel and carbon steel were 0.86 ± 0.05 and 0.54 ± 0.03 respectively.

Figure 5.12b shows the COF when sliding wear tests was performed under alumina ceramic counterface. For all slider materials, reduction in the friction coefficient was observed. The COF of the sintered sample when slid under $Al_2O_3$ counterface was 0.61 ± 0.05, approximately 27% lower than that when compared to sliding against stainless steel. This lower friction coefficient could possibly be attributed to the dissimilar tribo-pair, interface temperature generated between the pairs during sliding, surface roughness of the counterfaces, and the difference in the nature of wear debris layers. The COF values are summarized in the table 5.2.

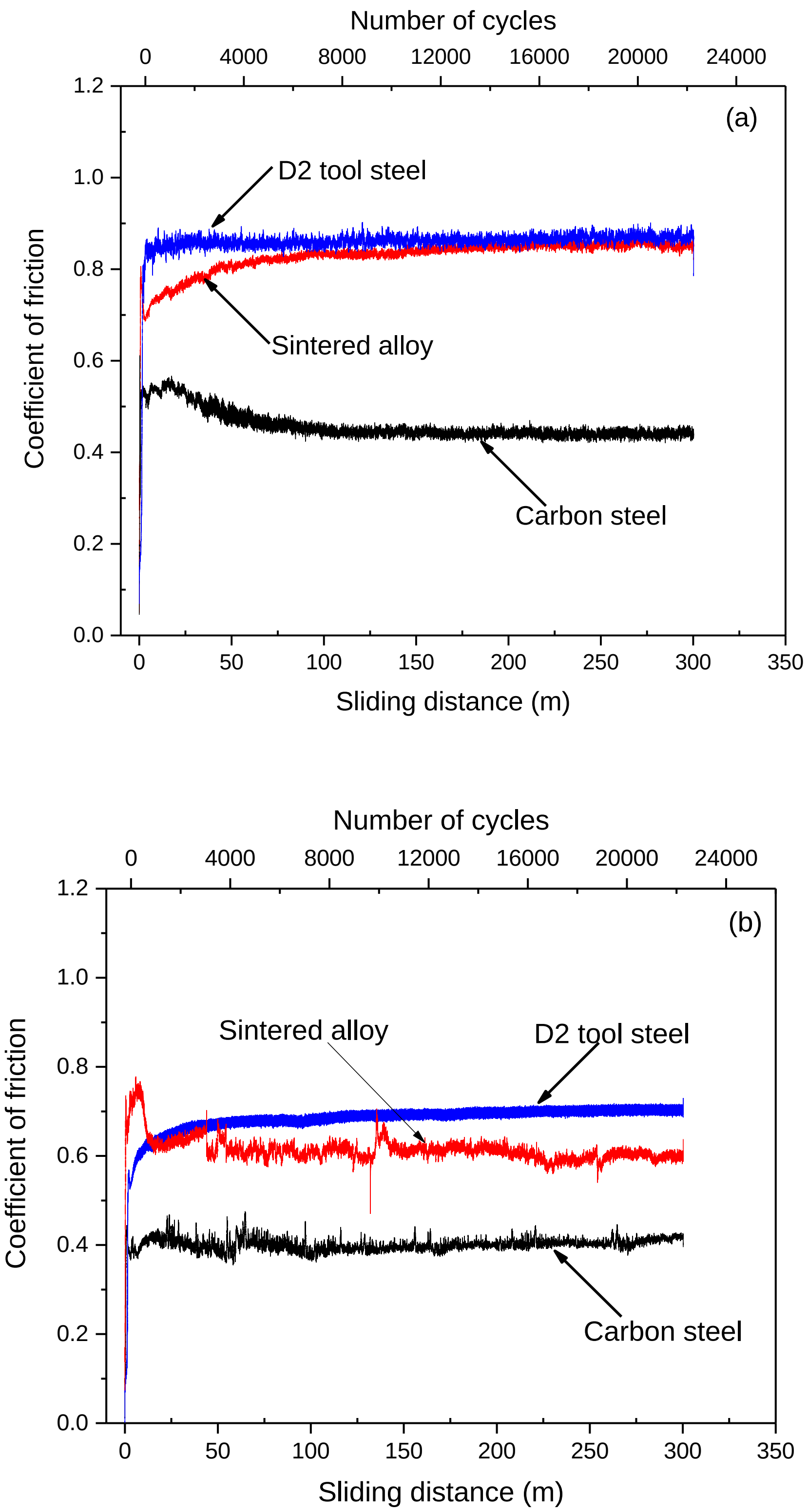

Figure 5.12. COF for sintered sample, D2 tool and carbon steel when slid against (a) stainless steel and (b) alumina counterface

Table 5.2. Steady state coefficient of friction values

| Steady state coefficient of friction | | |
|---|---|---|
| | Counterface materials | |
| | Stainless steel | Alumina |
| Slider materials | | |
| Sintered alloy | 0.837 ± 0.049 | 0.607 ± 0.045 |
| Carbon steel | 0.537 ± 0.028 | 0.402 ± 0.028 |
| D2 tool steel | 0.863 ± 0.047 | 0.697 ± 0.040 |

Figure 5.13a presents the wear volume results as a function of sliding distance for the carbon steel, D2 tool steel and sintered sample when slid against stainless steel counterface. For all samples, the wear volume is directly proportional to the sliding distance, which obeys the Archard's rule of adhesive wear. A similar trend of the result is reported [80,88]. The carbon steel exhibited maximum volume loss while the tool steel and sintered sample had the minimum and approximately equal volume loss. After about 24000 cycles (300 m of sliding wear test), the sintered sample exhibited about 84% lesser wear volume than carbon steel and 17% lesser wear volume than D2 tool steel, therefore, an evidence of a better wear resistance for longer sliding distance. The sintered sample has the highest hardness probably due the presence of the boride and carbide phases. The Archard's law proposing an indirect relationship between volume loss and hardness is apparent from the volume loss behavior. Furthermore, the wear rate, otherwise called the dimensional wear coefficient, *k* [89] of the slider materials was determined. The sintered alloy has a *k*-value of $1.90 * 10^{-6}$ mm$^3$ N$^{-1}$ m$^{-1}$ as compared with $1.22 * 10^{-5}$ mm$^3$ N$^{-1}$ m$^{-1}$ and $2.28 * 10^{-6}$ mm$^3$ N$^{-1}$ m$^{-1}$ for the carbon steel and D2 tool steel respectively.

Figure 5.13b presents the wear volume as a function of sliding distance for the sintered sample, D2 tool steel and carbon steel during sliding against alumina ceramic counterface. Similar to results as observed for testing against stainless steel, the wear volume increases linearly with sliding distance. After 300m of sliding wear, the sintered sample exhibited about 94% lesser wear volume than carbon steel, and 72% lesser wear volume than D2 tool steel, therefore, an evidence of a better wear resistance. Based on this information, the wear rate (dimensional wear coefficient, *k*) [89] of the sintered alloy is 3.52* $10^{-6}$ $mm^3$ $N^{-1}$ $m^{-1}$ compared with 1.24 * $10^{-5}$ $mm^3$ $N^{-1}$ $m^{-1}$ and 5.31 * $10^{-5}$ $mm^3$ $N^{-1}$ $m^{-1}$ for D2 tool steel and carbon steel respectively.

The wear volume of our spark plasma sintered Fe-based alloy when slid under stainless steel and alumina counterface was compared. An 86% increase in the wear volume and wear rate was observed for sliding against alumina as compared to stainless steel counterface. However, the sintered alloy had a better wear resistance when paired with alumina as compared to stainless steel counterface, which makes them viable as alumina cutting tools.

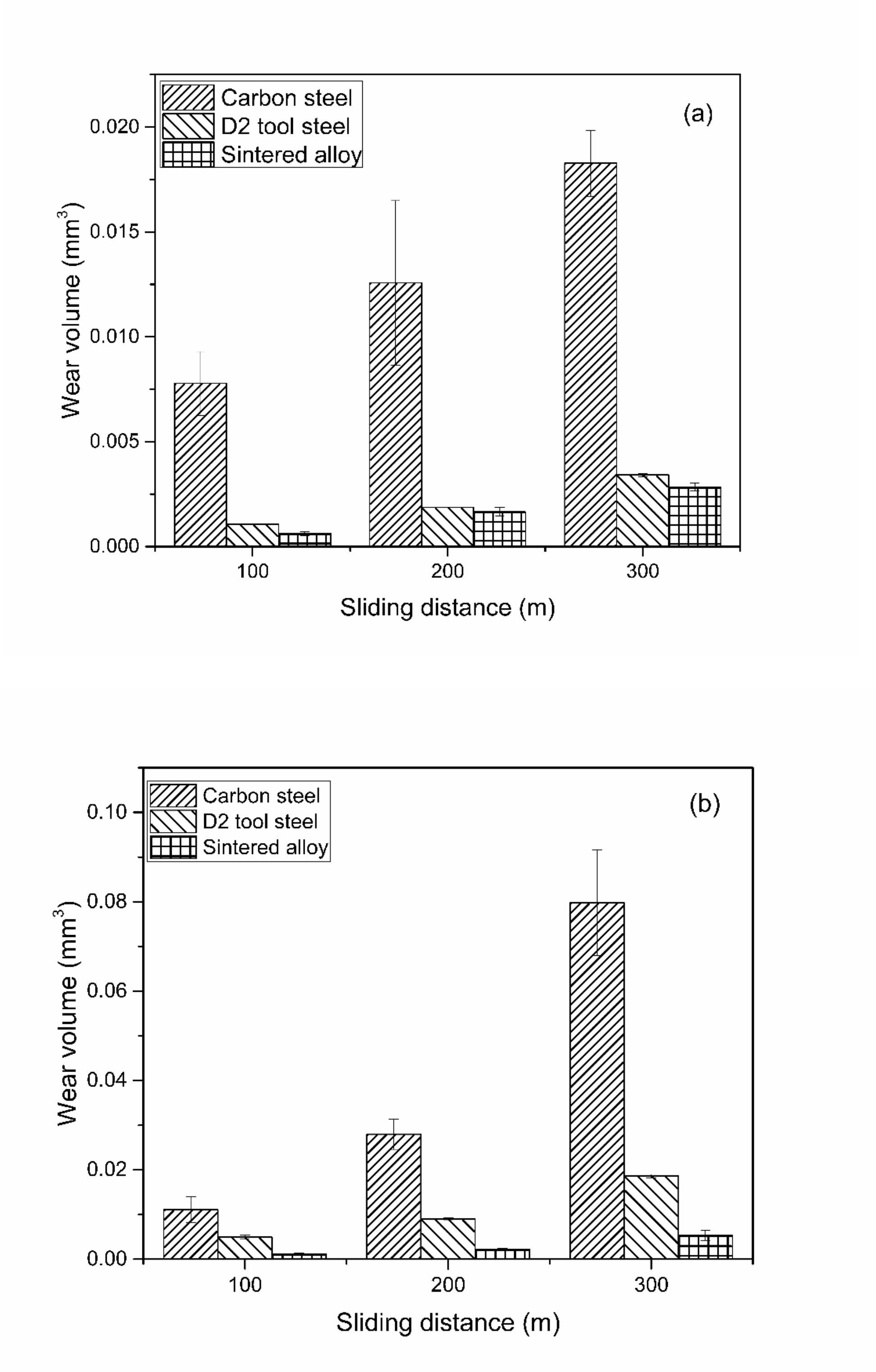

Figure 5.13. Plot showing the wear volume of sintered sample, D2 tool steel and carbon steel with sliding distance, when slid against (a) stainless steel and (b) alumina counterface.

Figure 5.14 shows micrographs of the wear scar of worn the stainless steel counterface. During sliding test the counterface also suffered some wear. The wear volume of the stainless steel counterface was determined and presented in Figure 5.15. Wear volume of stainless steel counterface was similar when the sintered alloy and tool steel were slid against it, whereas when carbon steel was slid against it, lesser wear of the counterface was experienced. This trend could be attributed to the hardness of the samples. The harder the tested sample, the more it wears the steel counterface.

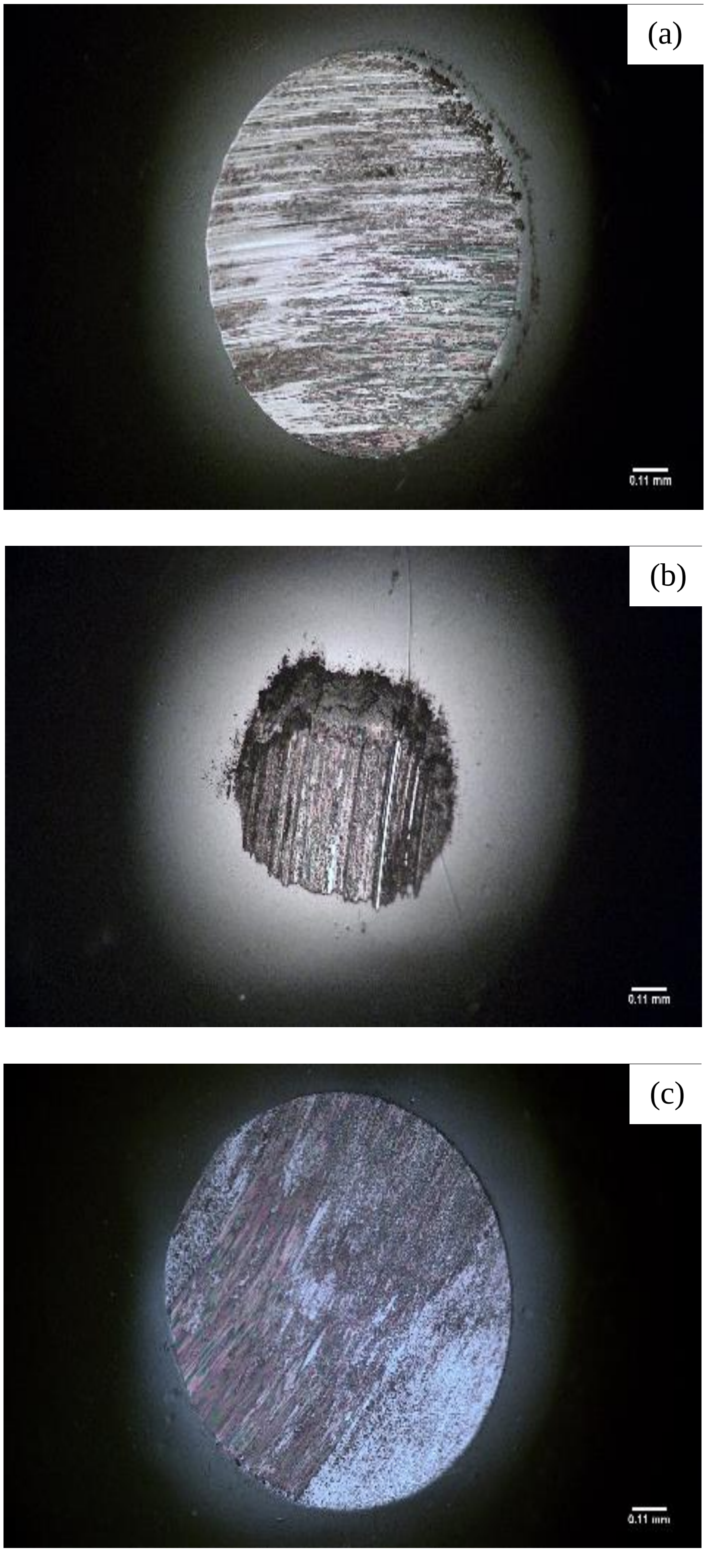

Figure 5.14. Typical optical images of the stainless steel counterface when the sintered alloy (a), carbon steel (b), and D2 tool steel (c) were slid against it.

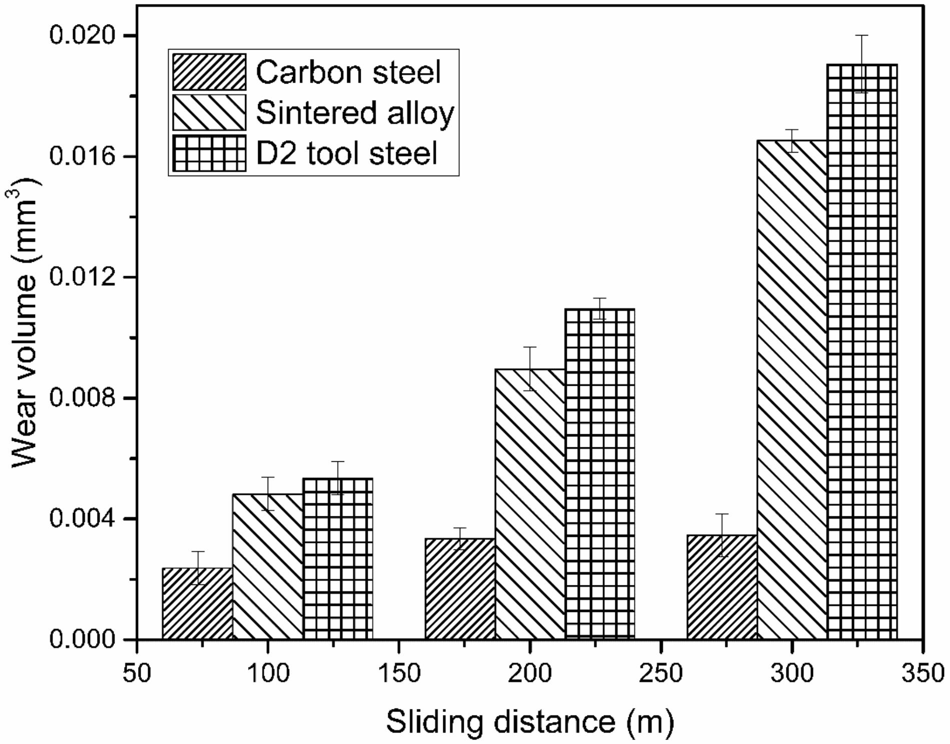

Figure 5.15. Plot showing the wear volume of stainless steel counterface when the sintered sample, D2 tool steel and carbon steel were slid against it.

The micrographs of the worn alumina counterface during the sliding wear test is also presented in figure 5.16. Although it is difficult to measure the diameter of the scar image, it is apparent that the size of wear scar was the most for the alumina counterface on the carbon steel (signifying more wear of the counterface), and the least for the alumina counterface on the sintered sample (less wear of the counterface).

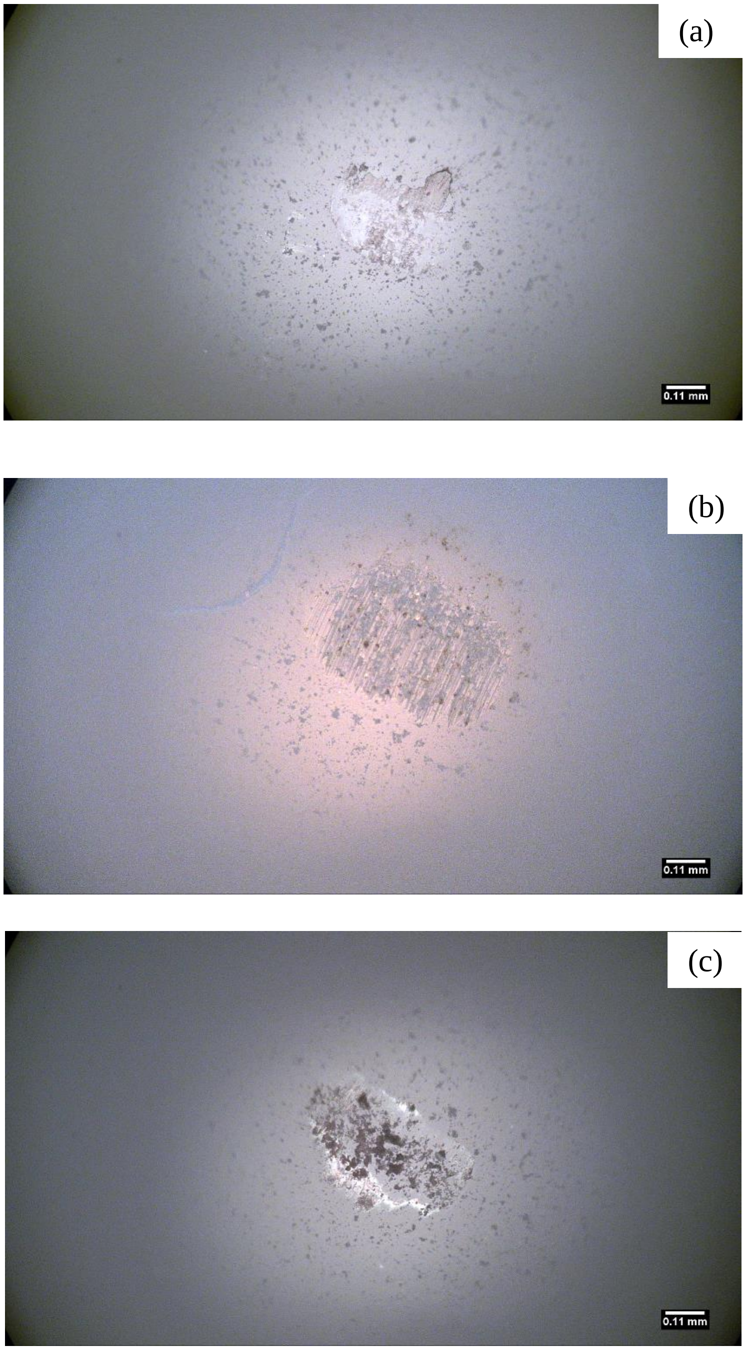

Figure 5.16. Typical optical images of the alumina counterface when the sintered alloy (a), carbon steel (b), and D2 tool steel (c) were slid against it.

### 5.3.4 Wear behavior

After sliding wear tests, microstructural investigation of the wear tracks and debris was evaluated to understand wear behavior of the sintered Fe-Cr-Mo sample. After 300 m of sliding wear against stainless steel and alumina counterfaces, SEM equipped with an EDS was used to investigate the worn surfaces and wear debris formed, and the resulting morphology is presented in figures 5.17 and 5.18.

Figure 5.17a (lower magnification) presents the worn surface of the sintered alloy after sliding against stainless steel counterface. Figure 5.17b shows the magnified micrograph. From the worn surfaces of the alloy, large amount of oxides were observed. These oxide rich region indicated oxidation reaction during sliding wear tests. EDS plots confirming the presence of these oxides is presented in figure 5.17c. Furthermore, the presence of grooves (parallel to the direction of sliding were observed) indicating a plowing mechanism of abrasive wear. EDS chemical analysis of the grooves showed that the region had less amount of oxidation as compared to other region. This area was rich in the main constituents of the MG alloy (Fe, Cr, and Mo).

Figure 5.18a (lower magnification) presents the wear track of the sintered alloy after sliding against alumina counterface. Figure 5.18b shows the magnified micrograph. From the worn surfaces of the alloy, large amount of oxides having flake-like shapes were observed. EDS spectrum confirming the oxide is presented in Figure 5.18c. The presence of these oxides indicated oxidative mechanism of sliding wear. The flatter regions of the wear track was rich in the major constituent elements of the alloy with a reduced amount of oxides. From the worn surface of the sample slid against alumina, wavy microcracks were observed. Similar microcracks have also been reported for other materials [80,82,90]. Wear debris which are highly rich in oxygen are presented in figure 5.19. Oxidation is usually responsible for formation of hard debris which leads to transition from sliding to abrasive wear. The proposed wear mechanisms thus are abrasive, adhesive wear and mild oxidation.

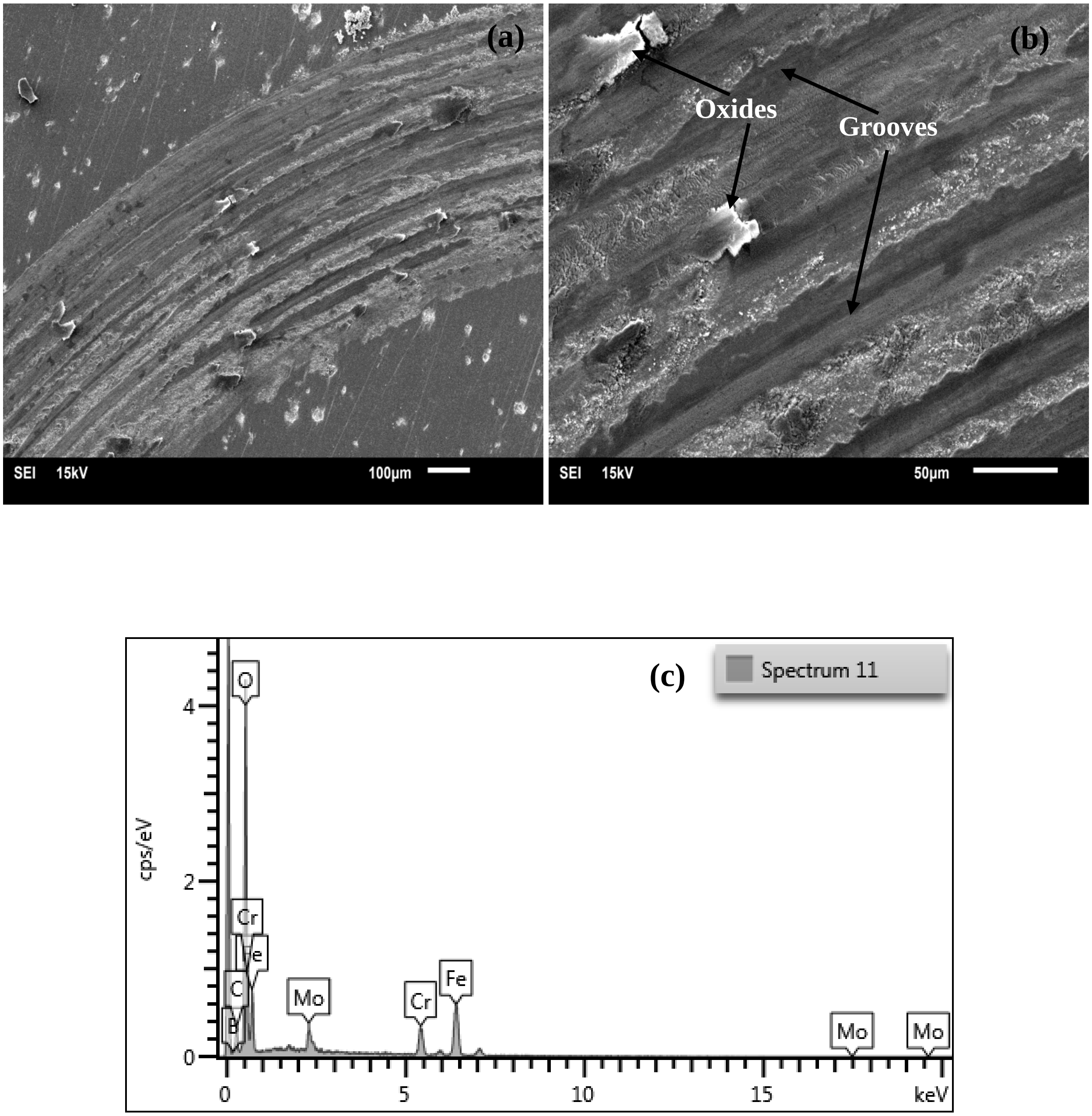

Figure 5.17. SEM-SE images and EDS plot from the worn surface of the sintered Fe-Cr-Mo alloy when slid against stainless steel counterface with the EDS plot corresponding to the oxide particle.

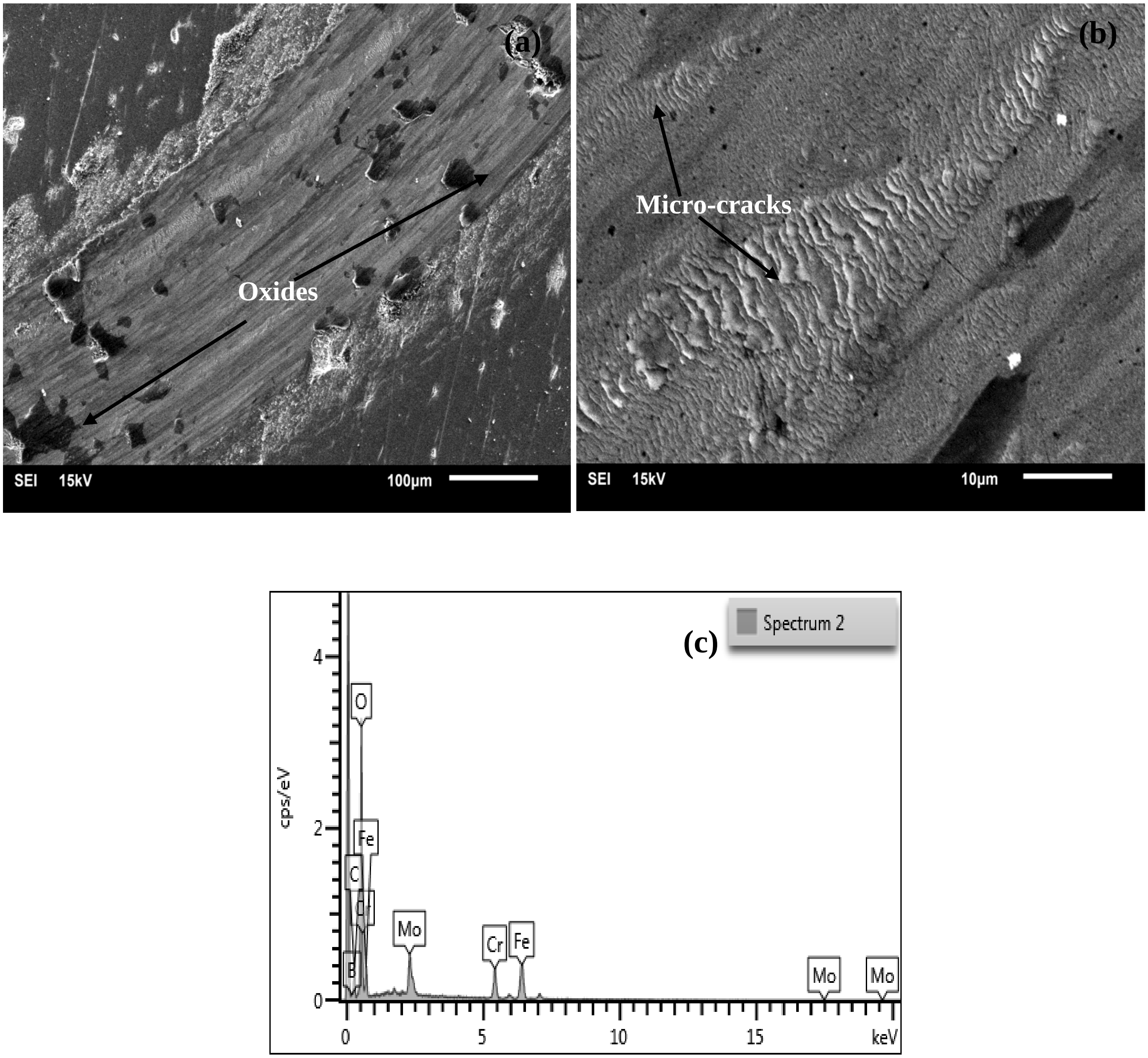

Figure 5.18. SEM-SE images and EDS plot from the worn surface of the sintered Fe-Cr-Mo alloy when slid against alumina counterface with the EDS plot corresponding to the oxide particle.

SEM SE micrographs showing the morphology and composition of wear debris is presented in figure 5.19a-b. Debris formed as a result of sliding against stainless steel and alumina counterparts had a similar elemental composition with high oxide content as shown in figure 5.19c. Debris was deposited both in the wear track and outside the track. The wear debris consisted of micrometer-sized flake-like particles and agglomerates. EDS mapping analysis also confirming the oxide-rich debris formed is presented in figure 5.20. The elemental distribution shows the oxide-rich debris concentrated at a location while other elements around the debris were uniformly distributed.

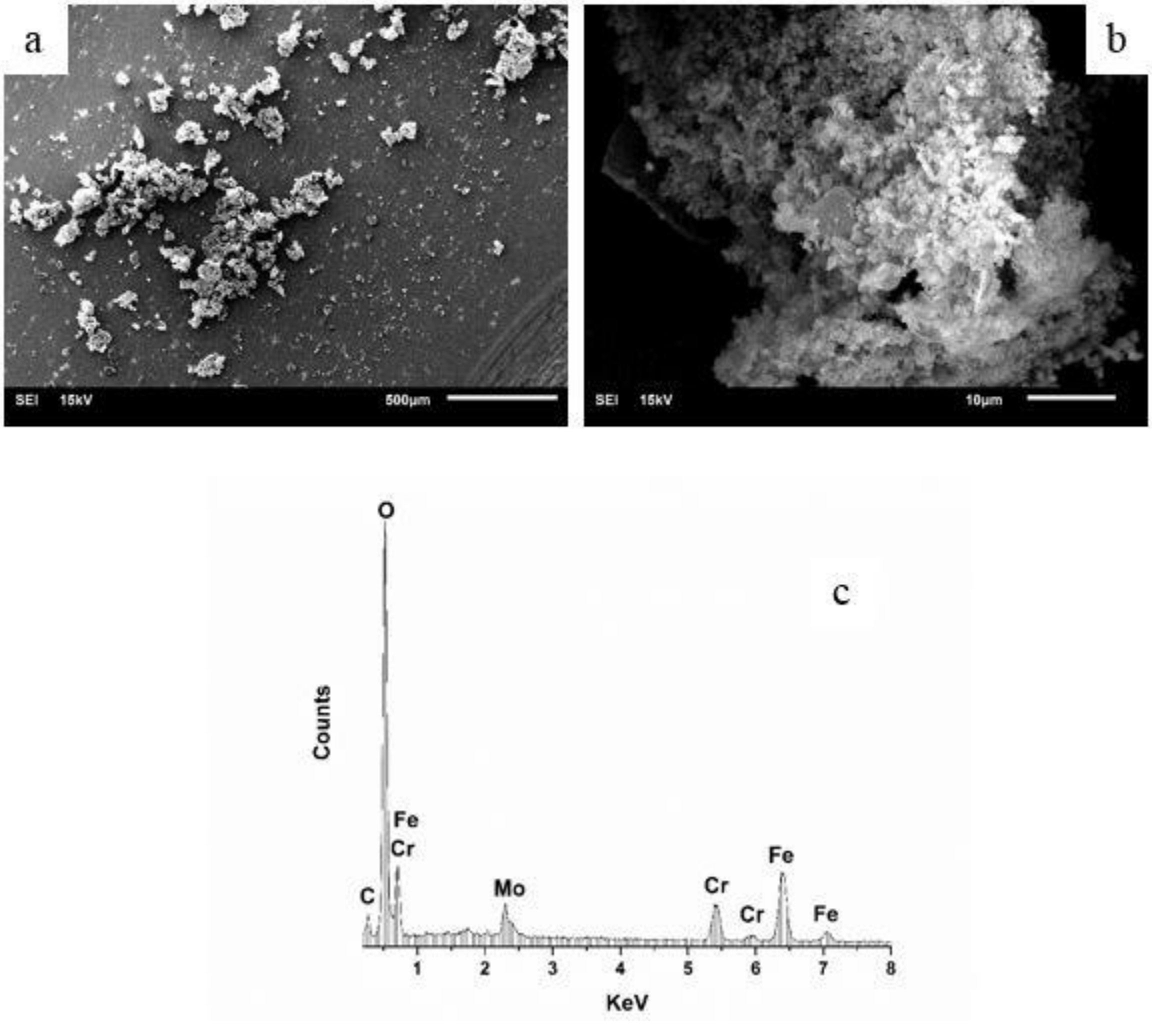

Figure 5.19. SEM-SE images of wear debris at low (a) and high (b) magnification when Fe-Cr-Mo alloy when slid against stainless steel ball. And EDS of debris (c)

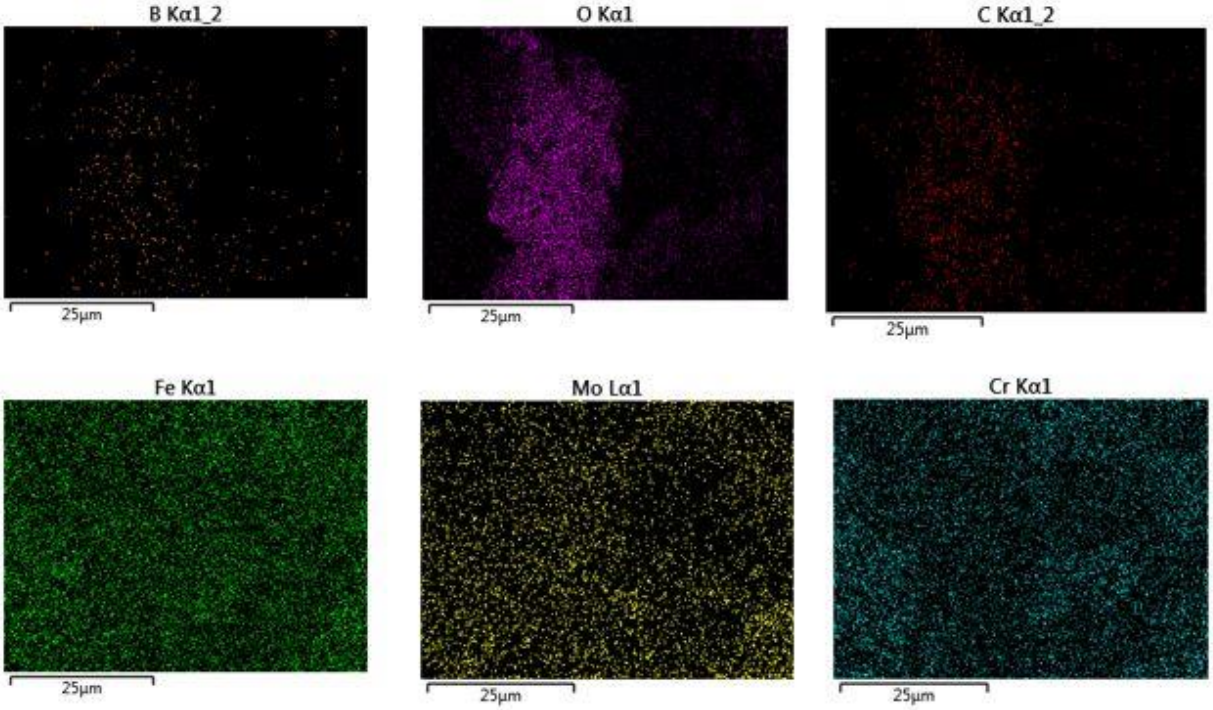

Figure 5.20. EDS mapping of wear debris particle

# CHAPTER 6

# CONCLUSIONS AND RECOMMENDATIONS

## 6.1 Conclusions

The $Fe_{58}Cr_{23}Mo_{15}B_2C_2$ (wt. %) metallic glass powders were consolidated using SPS processing method in order to investigate the effect of sintering temperature on the microstructure evolution and densification, and also to study the tribology of the sintered alloys. Based on this study the following conclusions are drawn:

I. As-received alloy powder was successfully consolidated using spark plasma sintering process. Relative density increased with sintering temperature. The samples sintered above the Tx had minimal porosities as compared to those sintered below Tx. Samples sintered below 700 °C showed low densification of about 85%, whereas those sintered at 900 and 1000 °C exhibited higher densification approximately 98%.

II. The consolidation of the Fe-based alloys resulted in a nanostructured material. At low sintering temperature of 500 and 600 $^{o}$C, small amounts of nanocrystalline $(Fe, Cr)_{23}C_6$ phase was observed in a background of an entirely amorphous phase. Crystallization increases with sintering temperature with the evolution of $(Fe, Cr)_{23}C_6$ particles and $(Cr, Fe)_2B$ nanoparticles embedded in a α-Fe (bcc) matrix. The crystallization of the alloy will lead to future understanding of the kinetics and micromechanisms of crystallization for Fe-based MG alloys.

III. The microhardness of the sintered samples increased with sintering temperature. While the hardness of samples sintered at 500, 600 and 700 $^{o}$C could not be determined, the hardness of the bulk samples sintered at 800 °C was observed to be lowest (837 HV) when compared the hardness of the samples sintered at 1000 °C (914 HV). The alloy sintered at 1000 $^{o}$C had the highest hardness because increased temperature is responsible for removal of porosity and better densification. The increased hardness is also due to the crystallization of carbide and boride phases, which in turn is responsible for the improved wear resistance.

IV. The coefficient of friction (COF)of the sintered alloy was 0.84 and 0.61 when slid against stainless steel and alumina ceramic counterface respectively. The sintered alloy exhibited a 27% reduction in COF when slid against alumina ball. Conventional carbon steel had lower steady state COF while D2 had higher steady state COF when compared to the sintered alloy.

V. When the sintered sample slid against stainless steel, its wear rate was 46% lower than that when it was slid against alumina ceramic ball. Generally, the sintered alloy had a higher wear resistance when compared with the conventional carbon steel and tool steel materials.

VI. After sliding tests under different ball materials, the primary wear mechanism were abrasion and mild oxidation.

## 6.2 Recommendations

The following recommendations for future work are proposed:

I. The successfully fabricated and highly dense samples were sintered above crystallization temperature and at a relatively low pressure. However, these samples had crystalline structures. It will therefore be important to sinter these amorphous powders at lower temperatures and high pressures and obtain highly dense compacts while retaining their noncrystalline structure. Other fabrication techniques such as microwave sintering, coating deposition could be explored.

II. In this study, wear properties of the sintered samples were compared to those of conventional materials. It will be important to study and understand the friction and wear behavior of these Fe-Cr-Mo alloys when fully amorphous, partially crystalline and fully crystalline. This knowledge is important in understanding the importance of bulk metallic glasses.

III. Wear studies in this research were done at a load of 5 N and a linear speed of 0.05 m/s. It will be important to study the wear behavior of the sintered Fe-Cr-Mo based alloy at lower and higher loads and speed in order to fully understand the alloy behavior under extreme and mild applications. In addition high temperature test, as well as sliding test under lubrication should be investigated to fully understand the alloy behavior.

IV. Soft magnetic properties should be investigated based on report of alloy systems in this range have been reported to possess this characteristics to be used as transformers, magnetic heads, induction coils and saturable reactors for nanocrystalline iron based alloys (because of their advantage of low eddy current losses).

# REFERENCES

[1] M.E. McHenry, M.A. Willard, D.E. Laughlin, Amorphous and nanocrystalline materials for applications as soft magnets, Prog. Mater. Sci. 44 (1999) 291–433. doi:10.1016/s0079-6425(99)00002-x.

[2] C. Suryanarayana, C.C. Koch, Nanocrystalline materials - Current research and future directions, Hyperfine Interact. 130 (2000) 5–44. doi:10.1023/A:1011026900989.

[3] H. Gleiter, Nanocyrstalline Materials, Prog. Mater. Sci. 33 (1989) 223–315. doi:10.1016/0079-6425(89)90001-7.

[4] P. Duwez, A typical example of metastability: Metallic glasses, J. Vac. Sci. Technol. B. 1 (1983) 218–221.

[5] M.M. Trexler, N.N. Thadhani, Mechanical properties of bulk metallic glasses, Prog. Mater. Sci. 55 (2010) 759–839. doi:10.1016/j.pmatsci.2010.04.002.

[6] W.H. Wang, C. Dong, C.H. Shek, Bulk metallic glasses, Mater. Sci. Eng. R Reports. 44 (2004) 45–90. doi:10.1016/j.mser.2004.03.001.

[7] M. Telford, The case for bulk metallic glass, 2004.

[8] M. Chen, A brief overview of bulk metallic glasses, NPG Asia Mater. 3 (2011) 82–90. doi:10.1038/asiamat.2011.30.

[9] A.L. Greer, E. Ma, Bulk Metallic Glasses: At the Cutting Edge of Metals Research, MRS Bull. 32 (2007) 611–619. doi:10.1557/mrs2007.121.

[10] C. Suryanarayana, A. Inoue, Iron-based bulk metallic glasses, Int. Mater. Rev. 58 (2012) 131–166. doi:10.1179/1743280412Y.0000000007.

[11] X.J. Gu, S.J. Poon, G.J. Shiflet, Mechanical properties of iron-based bulk metallic glasses, J. Mater. Res. 22 (2007) 344–351. doi:10.1557/jmr.2007.0036.

[12] G. Xie, Spark Plasma Sintering: A Useful Technique to Develop Large-Sized Bulk Metallic Glasses, J Powder Met. Min. 2 (2013) 2–4. doi:10.4172/2168-9806.1000e109.

[13] J.F. Löffler, Bulk metallic glasses, Intermetallics. 11 (2003) 529–540. doi:10.1016/S0966-9795(03)00046-3.

[14] A. Basu, A.N. Samant, S.P. Harimkar, J.D. Majumdar, I. Manna, N.B. Dahotre, Laser surface coating of Fe-Cr-Mo-Y-B-C bulk metallic glass composition on AISI 4140 steel, Surf. Coatings Technol. 202 (2008) 2623–2631. doi:10.1016/j.surfcoat.2007.09.028.

[15] A.L. Greer, Y.Q. Cheng, E. Ma, Shear bands in metallic glasses, Mater. Sci. Eng. R Reports. 74 (2013) 71–132. doi:10.1016/j.mser.2013.04.001.

[16] A. Singh, S.P. Harimkar, Spark plasma sintering of in situ and ex situ iron-based amorphous matrix composites, J. Alloys Compd. 497 (2010) 121–126. doi:10.1016/j.jallcom.2010.03.081.

[17] B. Movahedi, M.H. Enayati, C.C. Wong, On the crystallization behavior of amorphous Fe–Cr–Mo–B–P–Si–C powder prepared by mechanical alloying, Mater. Lett. 64 (2010) 1055–1058. doi:10.1016/j.matlet.2010.02.008.

[18] Z.A. Munir, U. Anselmi-Tamburini, M. Ohyanagi, The effect of electric field and pressure on the synthesis and consolidation of materials: A review of the spark plasma sintering method, J. Mater. Sci. 41 (2006) 763–777. doi:10.1007/s10853-006-6555-2.

[19] O. Guillon, J. Gonzalez-Julian, B. Dargatz, T. Kessel, G. Schierning, J. Räthel, et al., Field-assisted sintering technology/spark plasma sintering: Mechanisms, materials, and technology developments, Adv. Eng. Mater. 16 (2014) 830–849. doi:10.1002/adem.201300409.

[20] B.-T. Jang, S.-H. Yi, S.-S. Kim, Tribological behavior of Fe-based bulk metallic glass, J. Mech. Sci. Technol. 24 (2010) 89–92. doi:10.1007/s12206-009-1123-8.

[21] C. Jiang, Y. Xing, J. Hao, X. Song, Effects of heat-treatment on crystallization and wear property of plasma sprayed Fe-based amorphous coatings, J. Wuhan Univ. Technol. Sci. Ed. 28 (2013) 643–646. doi:10.1007/s11595-013-0744-z.

[22] D.H. Kwon, E.S. Park, M.Y. Huh, H.J. Kim, J.C. Bae, Wear behavior of Fe-based bulk metallic glass composites, J. Alloys Compd. 509 (2011) S105–S108. doi:10.1016/j.jallcom.2010.12.108.

[23] B.A. Singh, S.R. Paital, A. Andapally, N.B. Dahotre, S.P. Harimkar, Densification Behavior and Wear Response of Spark Plasma Sintered Iron-Based Bulk Amorphous Alloys **, (2012) 400–407. doi:10.1002/adem.201100322.

[24] D. Shechtman, I. Blech, D. Gratias, J.W. Cahn, Metallic phase with long-range orientational order and no translational symmetry, Phys. Rev. Lett. 53 (1984) 1951–1953. doi:10.1103/PhysRevLett.53.1951.

[25] R.C. Team, Scholar (3), (2014). doi:10.1163/_q3_SIM_00374.

[26] S. Suresh, A. Mortensen, A. Needleman, Fundamentals of Metal-matrix Composites, Butterworth-Heinemann, 1993.

[27] C. Suryanarayana, Nanocrystalline materials, Int. Mater. Rev. 40 (1994) 41–64. doi:10.1016/B978-0-12-407796-6.00009-9.

[28] M.A. Meyers, A. Mishra, D.J. Benson, Mechanical properties of nanocrystalline materials, Prog. Mater. Sci. 51 (2006) 427–556. doi:10.1016/j.pmatsci.2005.08.003.

[29] W. Klement, R.H. Willens, P. Duwez, Non-crystalline Structure in Solidified Gold-Silicon Alloys, Nature. 187 (1960) 869–870.

[30] H. Jones, A perspective on the developed of rapid solidification and nonequilibrium processing and its future, Mater. Sci. Eng. A. 304–306 (2001) 11–19. doi:10.1016/S0921-5093(00)01552-5.

[31] P. Duwez, A typical example of metastability: Metallic glasses, J. Vac. Sci. Technol. B Microelectron. Nanom. Struct. 1 (1983) 218–221. doi:10.1116/1.582490.

[32] A.C. Reardon, Discovering metals : a historical overview, Metall. Non-Metallurgist. 36 (2011) 73–84.

[33] C. Suryanarayana and Akihisa Inoue, Bulk metallic glasses, CRC Press, 2010.

[34] E. Arzt, Size effects in materials due to microstructural and dimensional constraints: a comparative review, Acta Mater. 46 (1998) 5611–5626. doi:http://dx.doi.org/10.1016/S1359-6454(98)00231-6.

[35] J.B. Cohen, The early stages of solute distribution below a transition temperature,

Metall. Trans. A. 23 (1992) 2685–2697. doi:10.1007/BF02651749.

[36] P.P. Choi, J.S. Kim, O.T.H. Nguyen, D.H. Kwon, Y.S. Kwon, J.C. Kim, Al-La-Ni-Fe bulk metallic glasses produced by mechanical alloying and spark-plasma sintering, Mater. Sci. Eng. A. 449–451 (2007) 1119–1122. doi:10.1016/j.msea.2006.02.264.

[37] B. V. Neamţu, T.F. Marinca, I. Chicinaş, O. Isnard, F. Popa, P. Păşcuţă, Preparation and soft magnetic properties of spark plasma sintered compacts based on Fe-Si-B glassy powder, J. Alloys Compd. 600 (2014) 1–7. doi:10.1016/j.jallcom.2014.02.115.

[38] H.Y. Jung, S.J. Choi, K.G. Prashanth, M. Stoica, S. Scudino, S. Yi, et al., Fabrication of Fe-based bulk metallic glass by selective laser melting: A parameter study, Mater. Des. 86 (2015) 703–708. doi:10.1016/j.matdes.2015.07.145.

[39] V.K. Balla, A. Bandyopadhyay, Laser processing of Fe-based bulk amorphous alloy, Surf. Coatings Technol. 205 (2010) 2661–2667. doi:10.1016/j.surfcoat.2010.10.029.

[40] C.C. Koch, Structural nanocrystalline materials: An overview, J. Mater. Sci. 42 (2007) 1403–1414. doi:10.1007/s10853-006-0609-3.

[41] Y. Yoshizawa, S. Oguma, K. Yamauchi, New Fe-based soft magnetic alloys composed of ultrafine grain structure, J. Appl. Phys. 64 (1988) 6044–6046. doi:10.1063/1.342149.

[42] K. Lu, J.T. Wang, W.D. Wei, A new method for synthesizing nanocrystalline alloys,

J. Appl. Phys. 69 (1991) 522–524.

[43] J.T. Wang, The structure and properties of nanocrystalline Fe78B138i 9 alloy, Science (80-. ). 150 (1992) 444–447.

[44] M.M. Nicolaus, H.R. Sinning, F. Haessner, Crystallization behaviour and generation of a nanocrystalline state from amorphous Co33Zr67, Mater. Sci. Eng. A. 150 (1992) 101–112. doi:10.1016/0921-5093(90)90012-R.

[45] P.O.F. Nanocrystalline, (Feo.99Moo.01) 788i9B13 ALLOYS, 28 (1993) 59–64.

[46] A.K. Singh, S.H. Alavi, S.R. Paital, N.B. Dahotre, S.P. Harimkar, Structural relaxation and nanocrystallization-induced laser surface hardening of fe-based bulk amorphous alloys, Jom. 66 (2014) 1080–1087. doi:10.1007/s11837-014-0974-3.

[47] M.A. Hussein, C. Suryanarayana, N. Al-Aqeeli, Fabrication of nano-grained Ti–Nb–Zr biomaterials using spark plasma sintering, Mater. Des. 87 (2015) 693–700. doi:10.1016/j.matdes.2015.08.082.

[48] M. Tokita, Mechanism of Spark Plasma Sintering, Proceeding NEDO Int. Symp. Funct. Graded Mater. (1999) 1–13.

[49] M. Suárez, a Fernández, J. Menéndez, Challenges and Opportunities for Spark Plasma Sintering: A Key Technology for a New Generation of Materials, Sinter. Appl. (2013). doi:10.5772/53706.

[50] J.E. Garay, Current-Activated, Pressure-Assisted Densification of Materials, Annu. Rev. Mater. Res. 40 (2010) 445–468. doi:10.1146/annurev-matsci-070909-104433.

[51] X.P. Li, M. Yan, H. Imai, K. Kondoh, J.Q. Wang, G.B. Schaffer, et al., Materials

Science & Engineering A bulk metallic glass with high fracture strength, 568 (2013) 155–159. doi:10.1016/j.msea.2013.01.041.

[52] G. Xie, D. V Louzguine-luzgin, M. Fukuhara, H. Kimura, A. Inoue, Intermetallics Cu particulate dispersed Cu 50 Zr 45 Al 5 bulk metallic glassy composite with enhanced electrical conductivity, Intermetallics. 18 (2010) 1973–1977. doi:10.1016/j.intermet.2010.02.043.

[53] C. Kyu, S. Lee, S. Yong, D. Hyang, Microstructure and mechanical properties of Cu-base amorphous alloy matrix composites consolidated by spark plasma sintering, 451 (2007) 924–928. doi:10.1016/j.msea.2006.02.326.

[54] C.Y. Son, C.K. Kim, S.Y. Shin, S. Lee, In situ microfracture observation of Cu-based amorphous alloy matrix composites containing copper or brass particles, Mater. Sci. Eng. A. 508 (2009) 15–22. doi:10.1016/j.msea.2009.01.038.

[55] F.O. Méar, G. Xie, D. V. Louzguine-Luzgin, A. Inoue, Spark Plasma Sintering of Mg-Based Amorphous Ball-Milled Powders, Mater. Trans. 50 (2009) 588–591. doi:10.2320/matertrans.MRA2008177.

[56] B. Zheng, D. Ashford, Y. Zhou, S.N. Mathaudhu, Influence of mechanically milled powder and high pressure on spark plasma sintering of Mg – Cu – Gd metallic glasses, 61 (2013) 4414–4428.

[57] J.K. Lee, H.J. Kim, T.S. Kim, S.Y. Shin, Y.C. Kim, J.C. Bae, Deformation behavior of Ni-based bulk metallic glass synthesized by spark plasma sintering, J. Mater. Process. Technol. 187–188 (2007) 801–804. doi:10.1016/j.jmatprotec.2006.11.206.

[58] G. Xie, D. V Louzguine-luzgin, H. Kimura, A. Inoue, Intermetallics Microstructure and mechanical properties of crystalline particulates dispersed Ni-based metallic glassy composites fabricated by spark plasma sintering, Intermetallics. 18 (2010) 851–858. doi:10.1016/j.intermet.2009.12.023.

[59] G. Xie, D. V. Louzguine-Luzgin, A. Inoue, Characterization of interface between the particles in NiNbZrTiPt metallic glassy matrix composite containing SiC fabricated by spark plasma sintering, J. Alloys Compd. 483 (2009) 239–242. doi:10.1016/j.jallcom.2008.07.226.

[60] G. Xie, W. Zhang, D. V. Louzguine-Luzgin, H. Kimura, A. Inoue, Fabrication of porous Zr-Cu-Al-Ni bulk metallic glass by spark plasma sintering process, Scr. Mater. 55 (2006) 687–690. doi:10.1016/j.scriptamat.2006.06.034.

[61] L. Perrière, M.T. Thai, S. Tusseau-Nenez, M. Blétry, Y. Champion, Spark plasma sintering of a Zr-based metallic glass, Adv. Eng. Mater. 13 (2011) 581–586. doi:10.1002/adem.201000334.

[62] S. Lee, H. Kato, T. Kubota, A. Makino, A. Inoue, Fabrication and soft-magnetic properties of Fe-B-Nb-Y glassy powder compacts by spark plasma sintering technique, Intermetallics. 17 (2009) 218–221. doi:10.1016/j.intermet.2008.07.021.

[63] O.A. Graeve, R. Kanakala, L. Kaufman, K. Sinha, E. Wang, B. Pearson, et al., Spark plasma sintering of Fe-based structural amorphous metals (SAM) with Y2O3 nanoparticle additions, Mater. Lett. 62 (2008) 2988–2991. doi:DOI 10.1016/j.matlet.2008.01.092.

[64] S.P. Harimkar, S.R. Paital, A. Singh, R. Aalund, N.B. Dahotre, Microstructure and

properties of spark plasma sintered Fe-Cr-Mo-Y-B-C bulk metallic glass, J. Non. Cryst. Solids. 355 (2009) 2179–2182. doi:10.1016/j.jnoncrysol.2009.07.007.

[65] A. Singh, S. Katakam, J. Ilavsky, N.B. Dahotre, S.P. Harimkar, Nanocrystallization in spark plasma sintered Fe48Cr 15Mo14Y2C15B6 bulk amorphous alloy, J. Appl. Phys. 114 (2013). doi:10.1063/1.4817379.

[66] S. Ahmadi, H.R. Shahverdi, S.S. Saremi, Nanocrystallization of α -Fe Crystals in Fe 52 Cr 18 Mo 7 B 16 C 4 Nb 3 Bulk Amorphous Alloy, J. Mater. Sci. Technol. 27 (2011) 497–502.

[67] B. Movahedi, M.H. Enayati, C.C. Wong, Study on nanocrystallization and amorphization in Fe–Cr–Mo–B–P–Si–C system during mechanical alloying, Mater. Sci. Eng. B. 172 (2010) 50–54. doi:10.1016/j.mseb.2010.04.016.

[68] R. Babilas, R. Nowosielski, Iron - based bulk amorphous alloys, Arch. Mater. Sci. Eng. 44 (2010) 5–27.

[69] S.S. Joshi, J.Z. Lu, N.B. Dahotre, Optimization of laser thermal treatment of Fe–Si–B metallic glass, J. Manuf. Process. 24 (2016) 31–37. doi:10.1016/j.jmapro.2016.07.004.

[70] R. Nowosielski, R. Babilas, G. Dercz, L. Pająk, Structure of Fe-Based Metallic Glass after Crystallization Process, Solid State Phenom. 163 (2010) 165–168. doi:10.4028/www.scientific.net/SSP.163.165.

[71] K.R. Ravi, Indumathi, R. Subramanian, B.S. Murty, Spark Plasma Sintering of Fe-Cr-Mo-P-B-C-Si Amorphous Alloy, Mater. Sci. Forum. 710 (2012) 320–325.

doi:10.4028/www.scientific.net/MSF.710.320.

[72] A. V. Sergueeva, D.J. Branagan, A.K. Mukherjee, Microstructure/properties relationship in Fe-based nanomaterials, Mater. Sci. Eng. A. 493 (2008) 237–240. doi:10.1016/j.msea.2007.08.090.

[73] S.J. Pang, T. Zhang, K. Asami, a. Inoue, Synthesis of Fe-Cr-Mo-C-B-P bulk metallic glasses with high corrosion resistance, Acta Mater. 50 (2002) 489–497. doi:10.1016/S1359-6454(01)00366-4.

[74] M.S. Bakare, K.T. Voisey, K. Chokethawai, D.G. McCartney, Corrosion behaviour of crystalline and amorphous forms of the glass forming alloy Fe43Cr16Mo16C15B10, J. Alloys Compd. 527 (2012) 210–218. doi:10.1016/j.jallcom.2012.02.127.

[75] S. Yoon, J. Kim, G. Bae, B. Kim, C. Lee, Formation of coating and tribological behavior of kinetic sprayed Fe-based bulk metallic glass, J. Alloys Compd. 509 (2011) 347–353. doi:10.1016/j.jallcom.2010.09.024.

[76] Q. Yang, R. Li, Z. Liu, M. Shi, X. Luo, T. Zhang, Compositional dependence of microstructure and tribological properties of plasma sprayed Fe-based metallic glass coatings, Sci. China Technol. Sci. 55 (2012) 1335–1342. doi:10.1007/s11431-012-4821-x.

[77] A. Singh, S.R. Bakshi, A. Agarwal, S.P. Harimkar, Microstructure and tribological behavior of spark plasma sintered iron-based amorphous coatings, Mater. Sci. Eng. A. 527 (2010) 5000–5007.

[78] A. Milanti, H. Koivuluoto, P. Vuoristo, G. Bolelli, F. Bozza, L. Lusvarghi, Microstructural Characteristics and Tribological Behavior of HVOF-Sprayed Novel Fe-Based Alloy Coatings, Coatings. 4 (2014) 98–120. doi:10.3390/coatings4010098.

[79] A. V. Kolomeichenko, I.S. Kuznetsov, Tribotechnical properties of electrospark coatings of amorphous and nanocrystalline iron alloys, J. Frict. Wear. 35 (2015) 501–504. doi:10.3103/S1068366614060087.

[80] D.R. Maddala, R.J. Hebert, Sliding wear behavior of Fe50-xCr15Mo14C15B6Erx (x=0, 1, 2 at%) bulk metallic glass, Wear. 294–295 (2012) 246–256. doi:10.1016/j.wear.2010.06.004.

[81] D.Z. Segu, Sliding Friction Properties of Bulk Metallic Glass in Seawater, (2015) 30–32.

[82] D.Z. Segu, J.H. Choi, S. Yi, S.S. Kim, Dry Sliding Tribological Properties of Fe-Based Bulk Metallic Glass, Tribol. Lett. 47 (2012) 131–138. doi:10.1007/s11249-012-9969-9.

[83] S.T. Method, Standard Test Method for Wear Testing with a Pin-on-Disk Apparatus 1, Wear. 5 (2011) 1–5. doi:10.1520/G0099-05R10.2.

[84] W. Yang, H. Liu, Y. Zhao, A. Inoue, K. Jiang, J. Huo, et al., Mechanical properties and structural features of novel Fe-based bulk metallic glasses with unprecedented plasticity, Sci. Rep. 4 (2014) 6233. doi:10.1038/srep06233.

[85] A.K. Melle, M.M. Peres, C. Bolfarini, W.J. Botta, A.M. Jorge Junior, C.S.

Kiminami, Consolidation of the Cu46Zr42Al7Y5 amorphous ribbons and powder alloy by hot extrusion, Mater. Res. 15 (2012) 728–731. doi:10.1590/S1516-14392012005000095.

[86] S. Shamsuddin, S.B. Jamaludin, Z. Hussain, Z.A. Ahmad, The effects of Al2O3 amount on the microstructure and properties of Fe-Cr matrix composites, Metall. Mater. Trans. A Phys. Metall. Mater. Sci. 41 (2010) 3452–3457. doi:10.1007/s11661-010-0414-0.

[87] J.C. Farmer, J.J. Haslam, S.D. Day, T. Lian, C.K. Saw, P.D. Hailey, et al., Corrosion resistance of thermally sprayed high-boron iron-based amorphous-metal coatings: Fe49.7Cr17.7Mn1.9Mo7.4W1.6B15.2C3.8Si2.4, J. Mater. Res. 22 (2007) 2297–2311. doi:10.1557/jmr.2007.0291.

[88] A.A. Sorour, H.W. Strauss, R.R. Chromik, M. Brochu, Microstructure and tribology of spark plasma sintered Fe-Cr-B metamorphic alloy powder, Tribol. Lett. 44 (2011) 269–278. doi:10.1007/s11249-011-9845-z.

[89] A.L. Greer, K.L. Rutherford, I.M. Hutchings, Wear resistance of amorphous alloys and related materials, Int. Mater. Rev. 47 (2002) 87–112. doi:10.1179/095066001225001067.

[90] D.Z. Segu, J.-H. Choi, S.S. Kim, Sliding wear behavior of Fe-based bulk metallic glass at high temperature, J. Mech. Sci. Technol. 26 (2012) 3565–3570. doi:10.1007/s12206-012-0855-z.

# VITAE

| | |
|---|---|
| Name | ADEDAYO SHERIFF ADENIYI |
| NATIONALITY | NIGERIAN |
| Date of Birth | 26/02/1988 |
| Email | adeniyi.adedayo.sheriff@gmail.com |
| Address | Lagos, Nigeria |
| Academic background | BSc. University of Lagos, Nigeria |